



PAPER

[View Article Online](#)
[View Journal](#) | [View Issue](#)Cite this: *J. Mater. Chem. A*, 2021, 9, 7068Fast lithium-ion conductivity in the 'empty-perovskite' $n = 2$ Ruddlesden–Popper-type oxysulphide $\text{Y}_2\text{Ti}_2\text{S}_2\text{O}_5^\dagger$ Kit McColl  [‡] and Furio Corà  ^{*}

Materials with Wadsley–Roth (W–R) crystallographic shear and bronze-type structures display fast lithium (Li)-ion diffusion and are of interest as anode materials for high-power Li-ion batteries. Here we use density-functional-theory calculations to investigate $\text{Y}_2\text{Ti}_2\text{S}_2\text{O}_5$, a Li-ion anode material that shares structural features with W–R phases. $\text{Y}_2\text{Ti}_2\text{S}_2\text{O}_5$ is a layered Ruddlesden–Popper-type oxysulphide displaying a reversible capacity of 128 mA h g^{-1} , with 60% capacity-retention at a charge rate of 20C in micrometer-sized electrode particles. The crystal structure contains an empty central layer of corner-sharing $[\text{TiO}_5\text{S}]$ octahedra, equivalent to a $(\infty \times \infty \times 2)$ block of the ReO_3 -like units that form Wadsley–Roth type phases. Intercalated Li^+ ions on this plane occupy distorted 'rectangular-planar' sites, and display 2D mobility with single-ion hopping barriers of 64 meV under dilute conditions. The insertion geometry of Li^+ is highly frustrated, giving rise to a smooth potential energy surface for Li-hopping and exceptionally low activation barriers. The $[\text{TiO}_5\text{S}]$ units do not experience major distortions or correlated rotations during discharge, due to framework rigidity provided by $[\text{Y}_2\text{S}_2]^{2+}$ rocksalt slabs, meaning the rectangular-planar-like geometry of Li^+ is retained across all states of charge. A tetragonal to orthorhombic to tetragonal phase change occurs upon lithiation, with a stable Li^+ ordering at $x = 1.0$ in $\text{Li}_x\text{Y}_2\text{Ti}_2\text{S}_2\text{O}_5$. Li^+ – Li^+ repulsion has a significant effect on the cation ordering at all Li intercalation levels. Na^+ hopping barriers are $>1.7 \text{ eV}$, while Mg^{2+} ions can move with barriers of $\sim 607 \text{ meV}$, illustrating the how diffusion behaviour varies for ions of different size and charge within W–R-type frameworks. The exceptionally low activation barriers for Li-hopping and well-defined, rigid 2D diffusion plane makes $\text{Y}_2\text{Ti}_2\text{S}_2\text{O}_5$ a valuable model system within which to understand Li^+ behaviour in high-rate electrode materials, such as the related Wadsley–Roth phases.

Received 21st November 2020
Accepted 15th February 2021

DOI: 10.1039/d0ta11358a

rsc.li/materials-a

Introduction

Next-generation lithium (Li)-ion batteries with fast charging and discharging times are required for improved performance of electric vehicles,^{1,2} and to aid load-smoothing for smart energy grids.³ Current Li-ion battery technology employs layered carbonaceous graphite anodes which are cheap and have long cycle-life.^{4,5} However, graphite anodes are poorly suited for high-power applications due to the formation of dendrites and

other unwanted side reactions at high (dis)charge rates that can result in catastrophic battery failure.^{6,7}

Crystalline transition metal oxides (TMOs) such as spinel $\text{Li}_4\text{Ti}_5\text{O}_{12}$ (LTO) are alternative anode materials to graphite and offer improved safety properties in high power applications, able to sustain higher rates without dendrite formation.^{8–11} Improved Li diffusion rates in crystalline TMOs are sought to achieve higher power densities. Higher diffusion rates can be achieved by nanosizing anode particles to shorten the diffusion lengths required to lithiate an entire anode material particle.² Such approaches have been successful in LTO,¹² but come at the cost of more complex synthesis, increased surface area causing faster degradation, and lower packing density.² The use of crystalline TMOs with intrinsically fast Li diffusion is therefore favourable for high power applications.

Recently, rapid lithium mobility has been identified in a selection of niobium-based complex oxides with open framework structures, including H- and T- Nb_2O_5 ,^{13–15} TiNb_2O_7 ,¹⁶ $\text{Nb}_{16}\text{W}_5\text{O}_{55}$ and $\text{Nb}_{18}\text{W}_{16}\text{O}_{93}$,¹⁷ $\text{PNb}_9\text{O}_{25}$ and $\text{VNb}_9\text{O}_{25}$ (ref. 18) and $\text{Nb}_{18}\text{W}_8\text{O}_{69}$.¹⁹ High charging and discharging rates can be achieved in many of these materials even in large, micrometer-

Department of Chemistry, UCL, London, WC1H 0AJ, UK. E-mail: f.cor@ucl.ac.uk

[†] Electronic supplementary information (ESI) available: Further details of the computational methods employed in the calculations; basis sets and constrained geometry optimisations for the calculations of activation barriers for ionic migration. Supplementary results; calculated crystal structure parameters for $\text{Y}_2\text{Ti}_2\text{S}_2\text{O}_5$ with different exchange–correlation functionals, and corresponding calculated bandgaps, calculated bond lengths for $\text{Y}_2\text{Ti}_2\text{S}_2\text{O}_5$ and calculated bond lengths in $[\text{TiO}_5\text{S}]$ octahedra for $\text{Li}_x\text{Y}_2\text{Ti}_2\text{S}_2\text{O}_5$. See DOI: 10.1039/d0ta11358a

[‡] Current address: Department of Chemistry, University of Bath, Bath, BA2 7AX, UK & Faraday Institution, Harwell Campus, Didcot, OX11 0RA, UK.

sized particles. They display low voltage vs. Li/Li^+ and as such, they are of interest as high-rate Li-ion anode materials. These materials have Wadsley–Roth (W–R) crystallographic shear, or structurally-related bronze-type frameworks (Fig. 1),²⁰ and their structural chemistry is thought to be key to the exceptional rate performance they display.

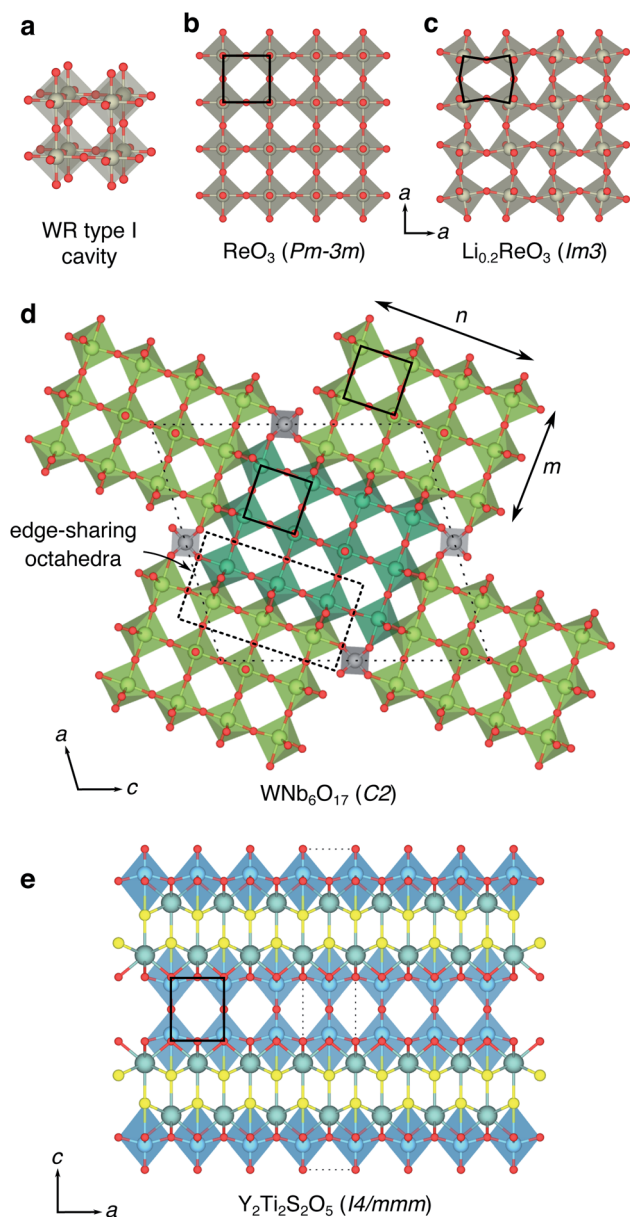


Fig. 1 Structural features of crystallographic shear phases and other related materials with Wadsley–Roth type framework units. (a) Type I cavity defined by a $(2 \times 2 \times 2)$ unit of corner-sharing $[\text{MO}_6]$ octahedra. (b) Structure of cubic ReO_3 ($Pm\bar{3}m$). The black line shows type I cavity, defining a (2×2) block. (c) The structure of $\text{Li}_{0.2}\text{ReO}_3$. The symmetry is lowered to $Im\bar{3}$. The black line shows distortion to the type I cavities. (d) Monoclinic ($C2$) structure of $\text{WNb}_6\text{O}_{17}$. Dark green and light green polyhedra indicate blocks offset by $b/2$. Grey tetrahedra are W ions. Solid black lines show $(2 \times 2 \times 2)$ units, which in $\text{WNb}_6\text{O}_{17}$ are capped by the edge-sharing octahedra to form a type II cavities. The dark dotted black line indicated edge-sharing octahedra, defining the edges of the $n \times m$ blocks. (e) Structure of $\text{Y}_2\text{Ti}_2\text{S}_2\text{O}_5$.

The structural units of the W–R-type phases were classified by Cava *et al.*, who identified six types of cavities within the frameworks.²¹ The basic building block is a cage-like unit, derived from the structure of cubic ReO_3 , consisting of four $[\text{MO}_6]$ octahedra sharing corners in a $(2 \times 2 \times 2)$ block, and defined by Cava *et al.* as a type I cavity (Fig. 1a and b). Type II cavities are found at shear-planes, when a ReO_3 -like unit is ‘capped’ by a pair of octahedra, edge-sharing with the block (Fig. 1d). Type III–VI cavities consist of more complex arrangements of polyhedra, and can include tetrahedrally-coordinated framework cations.²¹

The ‘empty-perovskite’, cubic ReO_3 is the simplest structure that can be formed from the W–R-type units defined by Cava *et al.*, constructed from only type I cavities, and is a model system for Li-ion intercalation in W–R-type materials (Fig. 1a and b). Li-ions can be introduced into the open cavities of ReO_3 and under dilute conditions they move with low activation barriers, leaving the framework relatively undisturbed.²² However, progressive intercalation of Li^+ causes correlated rotations of the corner-sharing octahedra (Fig. 1c) and a loss of the cubic framework, greatly increasing activation barriers and eventually leading to structural degradation on cycling.^{23–25} Similar distortions and structural degradation are observed upon lithiation of the corner-sharing-octahedra frameworks of WO_3 (ref. 26) and NbO_2F .²⁷

More complex W–R crystallographic shear phases are formed of $n \times m$ blocks of corner-sharing octahedra that meet at shear planes, and extend infinitely in columns along the periodic direction normal to the $n \times m$ plane (Fig. 1d).^{20,21,28} These block-edges and corners contain edge-sharing octahedra units that form W–R cavities assigned the designations type II–VI by Cava *et al.*²¹ The edge-sharing units bestow structural rigidity, so that the W–R framework does not relax significantly during intercalation.^{14,17,21,29} This structural property is key to their performance in battery applications, and means the low activation barriers for Li diffusion are retained across different states of charge, leading to exceptional charging and discharging rates.^{14,17,19}

Computational and experimental studies have revealed that Li diffusion is very fast down the centre of the columns in W–R phases, where type I, II or III cavities are linked through corners of their constituent octahedra. However, the diffusion is slower into ‘pocket’-like sites at block edges formed by the corner-sharing motifs of type II and III cavities.^{19,29} Furthermore, Li-ion hopping is inhibited between blocks in W–R phases, leading to effectively 1D diffusion down the columns.^{29,30}

The implications are thus; whilst shear planes provide structural rigidity that is key to the high Li-ion diffusion across different states of charge, they also restrict Li-ion mobility to 1D channels and introduce sites which Li-ions are slower to transfer in and out of. An ideal W–R-type structure for fast Li-ion diffusion would have 2D or 3D Li-ion connectivity and would contain diffusion pathways through structural units that are connected by corner-sharing octahedra only, whilst retaining framework rigidity.

$\text{Y}_2\text{Ti}_2\text{S}_2\text{O}_5$ is a complex layered material, based upon the $n = 2$ Ruddlesden–Popper (R–P) framework (Fig. 1e).^{31–33} In a conventional R–P phase, with stoichiometry $\text{A}_{n+1}\text{B}_n\text{O}_{3n+1}$ (for $n \geq 2$), the corner-sharing framework of octahedra in the ‘perovskite’ layers



would be occupied by 12-coordinate A-site cations. In $\text{Y}_2\text{Ti}_2\text{S}_2\text{O}_5$, these units are empty, leaving a 2D plane of 'ReO₃-like' type I Wadsley–Roth cavities into which Li^+ , Na^+ and Mg^{2+} ions can be intercalated.^{34–38} Rocksalt-type layers between the type I cavities provide structural rigidity that prevents the correlated distortions observed in ReO₃. No type II, or higher classification W–R cavities are present; the structure into which Li intercalation takes place contains only type I units, but with 2D connectivity, rather than the 3D connectivity in ReO₃.

$\text{Y}_2\text{Ti}_2\text{S}_2\text{O}_5$ has been investigated as a anode material for a Li-ion battery, and has a low average intercalation voltage for Li^+ of +0.84 V vs. Li/Li^+ .³⁸ The structure can accommodate 2 Li^+ per formula unit, resulting in a theoretical capacity of 128 mA h g^{−1}. This can be reversibly achieved over 30 cycles in 1.9 mm electrodes, with a small first-cycle hysteresis. High-rate performance is displayed, with 78% capacity retention at 10C and 60% at 20C for carbon-free electrodes containing 30 μm -thick $\text{Y}_2\text{Ti}_2\text{S}_2\text{O}_5$ particles.³⁸ Neutron diffraction experiments indicate that inserted Li^+ ions occupy approximately square-planar 'window' sites in the 2D plane.³⁷ This is a similar insertion environment to those identified for Li^+ in the high-rate Wadsley–Roth-type phases from DFT calculations,^{29,30} suggesting that similar mechanisms are responsible for activating high Li^+ mobility in both types of materials.

In this work we use density-functional-theory (DFT) calculations to investigate behaviour of Li^+ , Na^+ and Mg^{2+} within $\text{Y}_2\text{Ti}_2\text{S}_2\text{O}_5$. We begin by detailing the structure of the pristine phase. We then examine Li^+ intercalation and mobility at dilute concentrations, and Li-ordering at different levels of intercalation. Next, we compare the behaviour of Li^+ with Na^+ and Mg^{2+} . Subsequently, we investigate the electronic structure of the pristine material. Finally, we discuss the structure–property relationships in $\text{Li}_x\text{Y}_2\text{Ti}_2\text{S}_2\text{O}_5$, how the Li-ion diffusion properties could be modified through doping or chemical substitution, and the relevance of the results in relation to other fast Li-ion conducting anode materials such as the Wadsley–Roth phases.

Computational methods

First-principles calculations were performed using the periodic density-functional-theory (DFT) code CRYSTAL17.³⁹ The performance of a range of different functionals was tested (ESI†). For the majority of results presented in this work, electronic exchange and correlation were approximated using the PBEsol functional.⁴⁰ Electronic structure properties (electronic density of states and band structure) were obtained by fully relaxing the structure using the screened hybrid-exchange functional HSE06,^{41,42} with Grimme's semiclassical D3 correction.⁴³ Details of structural properties and bandgaps obtained using other functionals are provided in the ESI.† Atom-centered Gaussian basis sets were used for all atoms, available from the CRYSTAL online database (www.crystal.unito.it), with the online label indicated in the ESI.† All-electron basis sets were used to describe the following atoms: Ti, S, O, Li, Na and Mg. An effective core pseudopotential was used for the Y atom. The Coulomb and exchange series were truncated with thresholds of 10^{-7} , 10^{-7} , 10^{-7} , 10^{-7} and 10^{-14} .⁴⁴ Reciprocal space was sampled using a Pack–Monkhorst net,⁴⁵ with

a shrinking factor of $IS = 8$ along each periodic direction, for a total of 75 k -points in the irreducible Brillouin zone of the primitive cell of $\text{Y}_2\text{Ti}_2\text{S}_2\text{O}_5$. Modified k -point grids were used for supercell calculations to ensure a consistent sampling of reciprocal space. The self-consistent field (SCF) procedure was performed up to a convergence threshold of $\Delta E = 10^{-7}$ hartree per unit cell. Full geometry optimizations (lattice parameters and atomic positions) were performed using the default convergence criteria in CRYSTAL17. Li^+ , Na^+ and Mg^{2+} mobility was examined in a $(2 \times 2 \times 1)$ expansion of the crystallographic unit cell, ensuring a distance of $>7 \text{ \AA}$ between periodic images. Activation barriers for ionic migration were determined using constrained geometry optimisations, with full details of the procedure described in the ESI.†^{46,47} Li-orderings during intercalation were examined by considering all symmetry-inequivalent configurations in $(1 \times 1 \times 1)$ and $(\sqrt{2} \times \sqrt{2} \times 1)$ expansions of the crystallographic unit cell.⁴⁸ Intercalation voltages, V , were computed using the Nernst equation, which is given by: $V = -\Delta G/zF$ where ΔG is the Gibbs free energy change, F is the Faraday constant and z is the charge transferred. Under the calculation conditions, 0 K and zero pressure, the Gibbs free energy change is equivalent to the internal energy, $\Delta G = \Delta E$. The intercalation voltages were therefore computed as:

$$V = -\frac{E(\text{Li}_{(x_1)}\text{Y}_2\text{Ti}_2\text{S}_2\text{O}_5) - E(\text{Li}_{(x_2)}\text{Y}_2\text{Ti}_2\text{S}_2\text{O}_5) - (x_1 - x_2)E(\text{Li})}{(x_1 - x_2)F} \quad (1)$$

for $x_1 > x_2$, where $E(\text{Li}_{(x_1)}\text{Y}_2\text{Ti}_2\text{S}_2\text{O}_5)$ and $E(\text{Li}_{(x_2)}\text{Y}_2\text{Ti}_2\text{S}_2\text{O}_5)$ are the energies of the lithiated and delithiated materials respectively, and $E(\text{Li})$ is the internal energy of metallic lithium. Crystal structures were visualised using the VESTA software.⁴⁹

Lattice-gas Monte-Carlo simulations were run using the Python lattice_mc code.^{50,51} A model of the sites that Li can occupy in the (001) plane of $\text{Li}_x\text{Y}_2\text{Ti}_2\text{S}_2\text{O}_5$ was constructed, employing a square 2-dimensional unit cell with lattice parameter $a = 3.76 \text{ \AA}$ and two equivalent sites labelled A and B with fractional coordinates $[0, 0]$ and $[0.5, 0.5]$. A 12×12 expansion of the unit cell was taken, for a total of 288 sites, and a network was formed, each site was connected to its 4 nearest neighbours of opposite type only. Mobile particles were distributed randomly across the 288 sites and simulations were performed across the full range of possible lithium stoichiometry, from a single particle on the lattice to a single vacancy. Double-occupancy of sites was forbidden, all sites were set to have equal energy, and the interaction between particles was modelled using a nearest-neighbour energy term only, of $n \times k_B T$ where $n = 0, 1, 2, 3$ and 4. Simulations were run using a Metropolis–Hastings Monte-Carlo algorithm for 1000 equilibration steps, followed by 10 000 production steps, and results were averaged over 5000 simulations to obtain good statistics.

Results and discussion

Crystal structure of $\text{Y}_2\text{Ti}_2\text{S}_2\text{O}_5$

Tetragonal $\text{Y}_2\text{Ti}_2\text{S}_2\text{O}_5$ can be described as an A-site cation-defective $n = 2$ Ruddlesden–Popper (R–P) structure, formed of



$[\text{Y}_2\text{S}_2]^{2+}$ rocksalt and empty $[\text{Ti}_2\text{O}_5]^{2-}$ slabs layered in the c crystallographic direction (Fig. 2a). The crystallographic unit cell (space group $I4/mmm$, no. 139) contains five symmetry unique atoms; one of each Y, Ti and S and two symmetry unique O atoms, denoted O1 and O2. The Ti-rich layers comprise pairs of $[\text{TiO}_5]$ square pyramids, inverted with respect to each other and sharing an O2-ion across their peak. The Ti-ions are also linked through O1-ions at the corners of their pyramid base, forming a square lattice when the structure is viewed along the c direction (Fig. 2b). The Y atoms in the rocksalt layers are nine-fold coordinate, through four Y–O1 bonds and four Y–S bonds

to anions in the same layer, and one longer Y–S' bond 'across' the rocksalt layers to the adjacent layer (Fig. 2c).

In an alternative interpretation of the structure, the Ti ions can be considered to be in a highly distorted octahedral $[\text{TiO}_5\text{S}]$ coordination, with a long interatomic distance (2.87 Å) to a single S atom neighbour at the 'base' of the octahedron (Fig. 2d). When assessed in this way the $[\text{TiO}_5\text{S}]$ units form a $(2 \times 2 \times 2)$ cage (Fig. 2e) that can be related to the ReO_3 -like type I cavity describe by Cava *et al.* in Wadsley–Roth type phases (Fig. 1).²¹ The ReO_3 -like cavity is tetragonally elongated by the distortions to the Ti octahedra in the c direction. As a result, the shapes of the 'horizontal' and 'vertical' windows are different (Fig. 2f). The square 'horizontal' window defined by four O1 ions has a width of 3.75 Å, corresponding to the a lattice parameter. The rectangular 'vertical' windows are defined by two O1 ions and two O2 ions, have a width of a and a height of 4.57 Å (from O1 to O1). The position of the $[\text{Y}_2\text{S}_2]^{2+}$ rocksalt slabs means that type I cavities of TiO_5S units in subsequent layers in the c direction are offset from each other, in an AB stacking regime. The Ti–O–S layers form a $(\infty \times \infty \times 1)$ slab of Wadsley–Roth type I cavities in the (001) plane (Fig. 2g).

Table S1† reports the crystal structural parameters and bandgap for $\text{Y}_2\text{Ti}_2\text{S}_2\text{O}_5$ calculated using a range of different functionals, with and without dispersion corrections. Dispersion compresses the structure, with the greatest change along the c direction, normal to the plane of the layers. Most heavily affected by the dispersion correction are the Y–S bonds between the layers, which contract by 0.13 Å (Table S2†), indicating that dispersion forces make a non-negligible contribution to the bonding between the layers.

The hybrid-exchange functionals B3LYP (20% Hartree–Fock (HF) exchange) and PBE0 (25% HF-exchange), give bandgaps of 2.45 eV and 2.85 eV respectively. Both hybrid functionals overestimate the experimentally-reported bandgap of 1.9 eV–2.0 eV.^{33,52} PBE finds a bandgap of 1.08 eV, underestimated with respect to experiment. The bandgap calculated with HSE06 is 2.16 eV, close to the value reported from experiment. The PBEsol functional was chosen for the calculation of structural and energetic properties, since it gives a good representation of the crystal structure, with small errors relative to experiment.

Li⁺ intercalation and mobility under dilute conditions

Li⁺ intercalation under dilute conditions. Neutron diffraction experiments show that Li⁺ ions in $\text{Li}_x\text{Y}_2\text{Ti}_2\text{S}_2\text{O}_5$ adopt an approximately square-planar geometry in the vertical 'window' sites in the slab of the empty Ti–O–S type I cavities,³⁷ rather than a 12-coordinated geometry in the centre of the cavity.

Our DFT investigation of Li⁺ insertion began at dilute Li⁺ concentrations, considering a single Li⁺ ion in a $(2 \times 2 \times 1)$ expansion of the crystallographic unit cell, composed of 88 host ions, corresponding to a stoichiometry of $\text{Li}_{0.125}\text{Y}_2\text{Ti}_2\text{S}_2\text{O}_5$. The stable location for a Li⁺ ion under these conditions is in a site close to a vertical 'window' (Fig. 3a). The Li-ion does not occupy the centre of the type I cavity, consistent with experiment.³⁷ Li⁺ ions introduced into the horizontal windows migrated to the vertical windows.

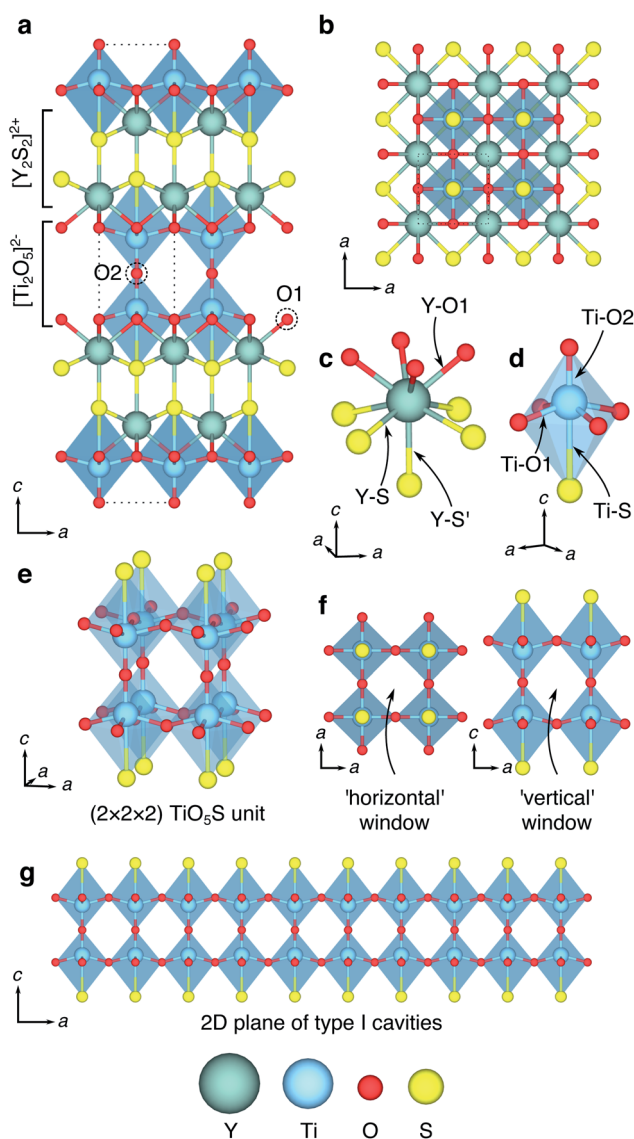


Fig. 2 Crystal structure of $\text{Y}_2\text{Ti}_2\text{S}_2\text{O}_5$. The tetragonal crystallographic unit cell of $\text{Y}_2\text{Ti}_2\text{S}_2\text{O}_5$, viewed along (a) the a direction and (b) the c direction. The dotted line shows a unit cell. The coordination environment of (c) Y atoms and (d) Ti atoms. (e) Structure of the empty ReO_3 -like central channel, formed of $(2 \times 2 \times 2)$ octahedra corner-sharing $[\text{TiO}_5\text{S}]$ units, related to the type I Wadsley–Roth cavities first designated by Cava *et al.*²¹ (f) Shape of the 'horizontal' and 'vertical' windows. (g) Illustration of the empty 2D central plane of $[\text{TiO}_5\text{S}]$ type I cavities for intercalation.



The Li^+ ions adopt a four-fold coordinated geometry, that is best described as distorted 'rectangular-near-planar'. Rather than sitting in an perfectly planar site flush in the 'window', directly in line with a O1 ion when the structure is viewed along the c direction, the Li^+ is displaced slightly into the type I cavity (Fig. 3b). The Li^+ ion binds to two O1 ions along the c direction with distances of 2.19 Å and 2.24 Å, and two O2 ions along the [001] plane of 1.90 Å (Fig. 3c). The distortion from a planar geometry is highlighted by the angle of the O1–Li–O1 bond along the c direction of 147.2° (Fig. 3d). Neutron diffraction experiments by Hyett *et al.* identified the Li-ion insertion sites as approximately 'square-planar', with large anisotropic displacement ellipsoids normal to the plane of the window.³⁷ The computational results presented here clarify that the equilibrium position for the Li-ions at 0 K is displaced slightly into the cavity, into the distorted 'rectangular-near-planar' sites. The distortion has important implications for the Li-ion potential energy surface, which are discussed later.

The displacement of the Li^+ -ion into the type I cavity in $\text{Y}_2\text{Ti}_2\text{S}_2\text{O}_5$ arises from the size and shape of the vertical 'window' site. The window is too narrow along the a direction to accommodate the Li perfectly, and it is 'squeezed' slightly into the cavity. A bond-valence sum calculation gives a value of $V_i = 0.88$ when the Li^+ ion is located in a planar rectangular site in the window. In contrast a value of $V_i = 0.99$ is found when the Li^+ ion is in the optimised position slightly into the cage.

Similar four-coordinate distorted square-planar-like Li^+ insertion geometry in 'window' positions has been reported from DFT calculations for selected sites within the Wadsley–

Roth-type Nb–W–O bronzes^{29,53} and TiNb_2O_7 ,³⁰ as well as in cubic ReO_3 under dilute conditions.²² It is notable that a square- or rectangular-planar-like arrangement is an unusual geometry for Li^+ . An ideal four-fold coordination for the stabilisation of an ion from a set of point charges is tetrahedral geometry, and whilst three-coordinate trigonal-planar Li^+ is described in KLiO ,⁵⁴ and a range of five-fold coordination environments are known, four-fold geometry such as square-planar is not discussed in reviews of Li^+ coordination chemistry in crystals.^{55,56}

Despite the distorted rectangular-near-planar site being a global minimum on the 0 K potential energy surface at this low level of lithiation, the Li^+ ions can be described as having a highly 'frustrated' coordination. The insertion geometry of the Li^+ ions is destabilised, in comparison to tetrahedral or octahedral geometries that are more commonly observed. 'Frustrated' coordination typically results in lower activation barriers for ion-hopping, since the destabilisation reduces the difference in energy between the initial site and the transition state.³⁷ The use of structures with 'frustrated' coordination has been proposed to improve ionic mobility for Li^+ and multivalent battery cathode materials.^{58,59}

Table 1 reports the crystal structure parameters for $\text{Li}_x\text{Y}_2\text{Ti}_2\text{S}_2\text{O}_5$ structures. Under dilute conditions of $x = 0.125$ the structure displays a slight orthorhombic distortion, with an expansion of the b lattice parameter by +0.3%. The structure also experiences a slight contraction of the c lattice parameter, by –0.9%.

Li^+ mobility under dilute conditions. Intercalated Li^+ ions move in 2D on the (001) plane. Two hopping pathways can be defined within the structure, due to the displacement of the Li^+ ions into the cage. Path 1 is a 'rattling' between two different sites either side of a vertical window (Fig. 4a). Sites labelled A and A' are equivalent, but separated by the plane of the window. Along path 2, Li^+ ions hop from a window site to an equivalent adjacent window site within the same cage (Fig. 4b), shown by A' and A''. Fig. 4c shows the two hopping pathways when the structure is viewed along the c direction.

The hopping barriers for paths 1 and 2 are shown in Fig. 4d. The activation barrier for the 'rattling' path 1 is 20 meV, and for path 2 the barrier is 64 meV. Comparatively low barriers have been reported from DFT calculations for similar hopping and rattling pathways in the Nb–W–O bronzes.²⁹ These values are amongst the lowest single-ion hopping barriers reported for Li^+ diffusion in an electrode or electrolyte materials. For comparison, activation barriers for single-ion hopping in the high-rate LiMn_2O_4 spinel cathode material are around 300 meV–400 meV,^{60,61} and barriers of 150 meV–300 meV are found in 'super-ionic' Li^+ -ion conducting electrolytes.^{62,63}

The very low activation barrier for the 'rattling' path 1 of 20 meV is consistent with neutron diffraction results presented by Hyett *et al.*³⁷ They reported highly elongated anisotropic displacement ellipsoids for the refined positions of Li^+ ions occupying approximately square-planar 'window' sites within $\text{Y}_2\text{Ti}_2\text{S}_2\text{O}_5$ for data collected at 298 K. The equilibrium geometry of Li at 0 K is slightly within the cavity. However, the activation barrier of 20 meV is below kT at 298 K (25.7 meV), thus a rattling motion of Li^+ ions along path 1 is expected to occur under

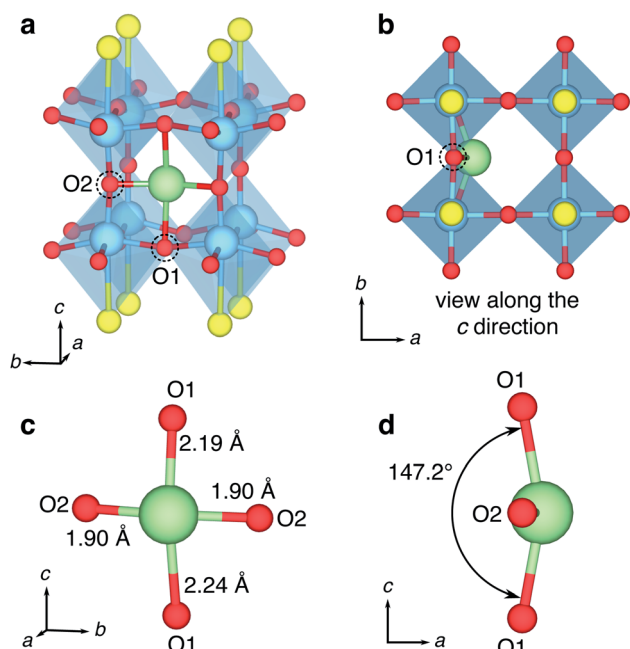


Fig. 3 Li^+ insertion geometry in $\text{Li}_x\text{Y}_2\text{Ti}_2\text{S}_2\text{O}_5$ under dilute conditions ($x = 0.125$). (a) Position of Li^+ in a 'window' site of a ReO_3 -like Ti–O–S 'cage'. (b) The structure viewed along the c direction, showing displacement slight into the 'cage'. (c) Li–O distances. (d) O1–Li–O1 angles.



Table 1 Lattice parameters for $\text{Li}_x\text{Y}_2\text{Ti}_2\text{S}_2\text{O}_5$ structures. Calculated structures along the ground state convex hull at $x = 0, 0.125, 0.5, 1, 1.5$ and 2 are compared with the closest matching stoichiometry reported from experiment.³⁷ The value in brackets is the % difference in the calculated structural parameter, with respect to the equivalent experimental structure

x	Method	Crystal system	a (Å)	b (Å)	c (Å)	Vol (Å ³)
0	Expt ³⁷	Tetragonal	3.770		22.806	324.06
	DFT		3.759 (−0.3%)		22.726 (−0.4%)	321.18 (−0.9%)
0.125	DFT	Orthorhombic	3.770	3.781	22.605	322.18
0.5	DFT	Orthorhombic	3.796	3.856	22.267	325.89
0.99	Expt ³⁷	Orthorhombic	3.832	3.919	22.301	334.88
1.00	DFT		3.842 (0.3%)	3.911 (−0.2%)	21.879 (−1.9%)	328.75 (−1.8%)
1.52	Expt ³⁷	Tetragonal	3.918		22.065	338.77
1.50	DFT		3.927 (0.2%)		21.541 (−2.4%)	332.13 (−2.0%)
1.85	Expt ³⁷	Tetragonal	3.943		21.958	341.31
2.00	DFT		3.952 (0.2%)		21.372 (−2.7%)	333.77 (−2.2%)

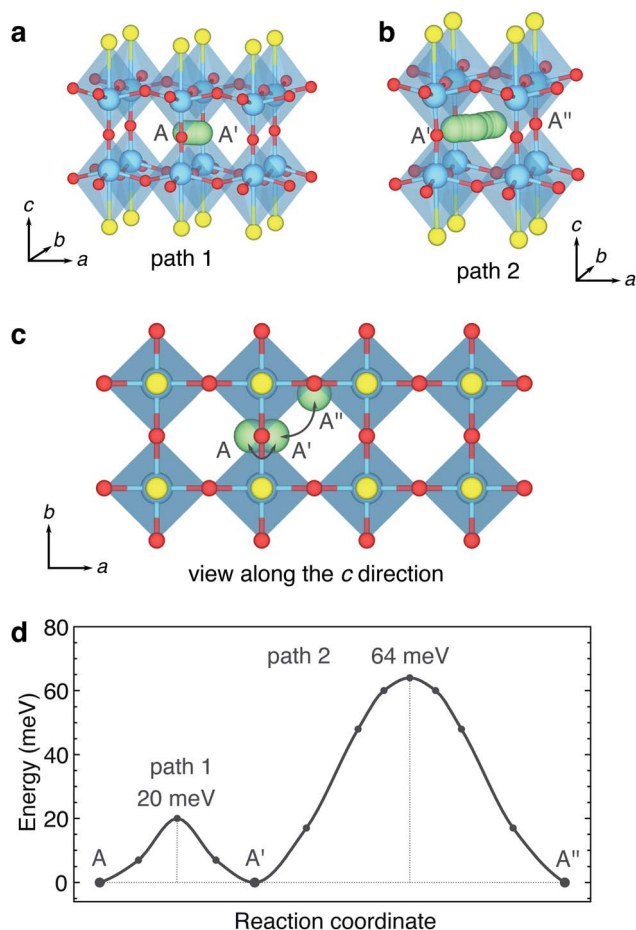


Fig. 4 Li^+ single-ion hopping pathways under dilute conditions. (a) Route for path 1, from sites $A \rightarrow A'$. (b) Route for path 2 from site $A' \rightarrow A''$. (c) View of paths 1 and 2 along the c axis. Note that the crystallographic directions a and b have been defined to indicate the orthorhombic distortion arising from the Li -ion in site A' . (d) Calculated activation barriers for paths 1 and 2 from DFT.

ambient conditions. Although Li^+ diffusion in $\text{Y}_2\text{Ti}_2\text{S}_2\text{O}_5$ will be heavily affected by correlated ion-hopping and ordering at non-dilute Li^+ concentrations, the low activation barriers at dilute concentrations suggests that the lithium diffusion will be rapid

across different states of charge. The low activation barriers are therefore consistent with the results of Oki and Takagi, who report high discharge rates of 1C–20C in 30 μm -size particles with excellent capacity retention.³⁸

$\text{Li}^+ - \text{Li}^+$ repulsion effects at low lithiation levels. To investigate the influence of $\text{Li}^+ - \text{Li}^+$ repulsion on site filling in $\text{Li}_x\text{Y}_2\text{Ti}_2\text{S}_2\text{O}_5$, we employed the same $(2 \times 2 \times 1)$ 88 host-ion cell. A second Li^+ was introduced into the same type I cavity as the first Li -ion (corresponding to $x = 0.25$), and the geometry of the system was optimised. Fig. 5 shows the final geometry of the system for two cases, where the Li is either introduced into an opposite window (Fig. 5a), or adjacent window (Fig. 5b). The initial geometry of the second Li in each case is indicated by a dotted circle, and the movement of the Li -ion by an arrow. In both cases, upon optimisation, the second Li -ion hops *via* path 1 through the closest window into a new site in the next cage. The hop is driven by the electrostatic repulsion between the two positive Li^+ ions within the same cavity, and this repulsion is enough to overcome activation barrier of 20 meV for path 1. $\text{Li}^+ - \text{Li}^+$ repulsion therefore has a strong effect on the cation ordering, inhibiting the double-occupation of one cavity. The lower-energy configuration sees the second Li^+ ion displaced

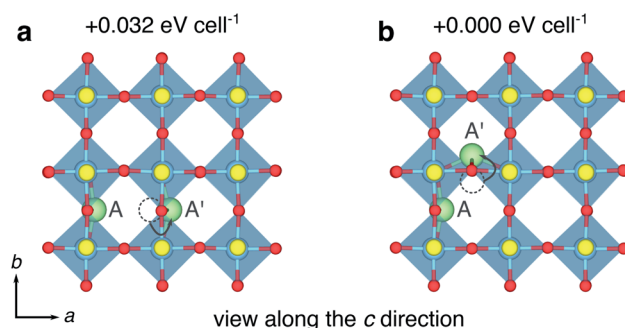


Fig. 5 The effect of $\text{Li}^+ - \text{Li}^+$ repulsion on nearest-neighbour site filling and energies at dilute concentrations. (a) Two Li -ion occupying window sites along the same $[010]$ direction. (b) Two Li -ion occupying window sites along the same $[110]$ direction. In both (a) and (b) the dashed circle represents an unstable site. A Li^+ ion introduced into this site hops into site A' *via* path 1. The b axis direction indicates the slight orthorhombic distortion to the structure, initiated by the introduction of the first Li^+ ion.



into the neighbouring cage in the adjacent window (Fig. 5b), rather than the opposite window (Fig. 5a), which is 32 meV higher in energy. As a result of the Li–Li repulsion, intercalation and site filling is expected to take place *via* a highly-correlated mechanism between $0 < x \leq 1$.

Ground state hull structures of $\text{Li}_x\text{Y}_2\text{Ti}_2\text{S}_2\text{O}_5$

Reports of chemical³⁷ and electrochemical³⁸ lithiation of $\text{Y}_2\text{Ti}_2\text{S}_2\text{O}_5$ exist in the literature. Electrochemical lithiation of $\text{Y}_2\text{Ti}_2\text{S}_2\text{O}_5$ vs. Li/Li^+ results in a sloping voltage curve with two distinct steps at $x = 1.0$ and $x = 1.5$.³⁸ Neutron diffraction experiments show that $\text{Li}_x\text{Y}_2\text{Ti}_2\text{S}_2\text{O}_5$ remains tetragonal during the initial stages of chemical Li^+ intercalation. At $x \approx 1$, a orthorhombic distortion and an ordering of Li^+ ions in parallel windows in the b direction is observed. The orthorhombic Li^+ ordering at $x = 1.0$ corresponds to the step in the voltage profile at $x = 1.0$.^{37,38} The tetragonal structure is recovered when $x > 1.52$.³⁷ In this section, we investigate structural changes and Li-orderings during the lithiation process between $0 \leq x \leq 2$.

Convex hull and voltage curve for $\text{Li}_x\text{Y}_2\text{Ti}_2\text{S}_2\text{O}_5$. Li distributions at different values of x in the limits $0 \leq x \leq 2$ in $\text{Li}_x\text{Y}_2\text{Ti}_2\text{S}_2\text{O}_5$ were calculated. From these, a convex hull of stability and voltage curve has been derived, shown in Fig. 6. The calculations identify four ground-state orderings along the convex hull between the pristine and fully lithiated states, at $x = 0.125$ and $x = 0.5$, $x = 1.0$, $x = 1.5$. There are a number of structures very close to the ground-state hull, at $x = 0.25$, $x = 0.75$ and $x = 1.75$, indicating a solid-solution type mechanism in action for most of the intercalation process. The calculated

lattice parameters of the ground-state structures are reported in Table 1, compared with the structural parameters for the closest experimentally-reported stoichiometry, showing good agreement.

The experimental voltage curve is gently sloping in profile, with three distinct sloped regions separated by small and slightly softened, but distinct voltage drops at $x = 1.0$ and $x = 1.5$. The calculated voltage curve captures the clear step at $x = 1.0$, and a step at $x = 1.5$. A number of structures are calculated close to the ground state hull and may be accessible at finite temperatures. Since intercalation occurs in smooth solid-solution mechanism, a finer evaluation of the voltage curve at varying x would require cluster-expansion-based Monte Carlo simulations.

Li ordering at $x = 1$ in $\text{Li}_x\text{Y}_2\text{Ti}_2\text{S}_2\text{O}_5$. Fig. 7 shows three high-symmetry structures for $\text{LiY}_2\text{Ti}_2\text{S}_2\text{O}_5$ ($x = 1$) within the unit cell. The ground state structure is orthorhombic (Fig. 7a). Here, half the Li-ions occupy each $[\text{TiO}_5\text{S}]$ type I cavity layer, are arranged in chains, and form Li–O bonds along the b axis causing an expansion of the unit cell in that direction. The Li-ions in each layer have an AB stacking. This structure is in agreement with the orthorhombic phase reported from chemical lithiation to $x = 0.99$ from experiment (Table 1),³⁷ and is likely to correspond to the ordered structure that appears as a distinct step in the experimental voltage curve at $x = 1$.³⁸ The next-lowest energy

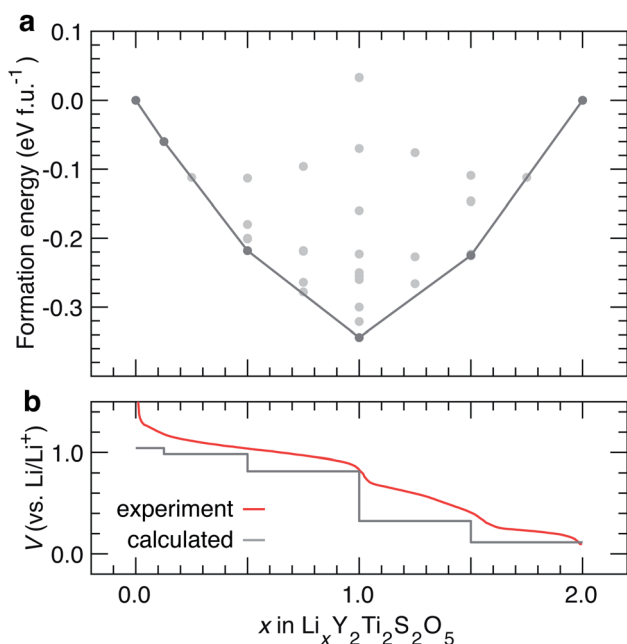


Fig. 6 (a) Convex hull for Li intercalation in $\text{Li}_x\text{Y}_2\text{Ti}_2\text{S}_2\text{O}_5$ between $0 \leq x \leq 2$. The structures along the ground state hull are reported in Table 1. (b) Corresponding calculated voltage curve, compared against the experimental voltage curve reported by Oki and Tagaki.³⁸

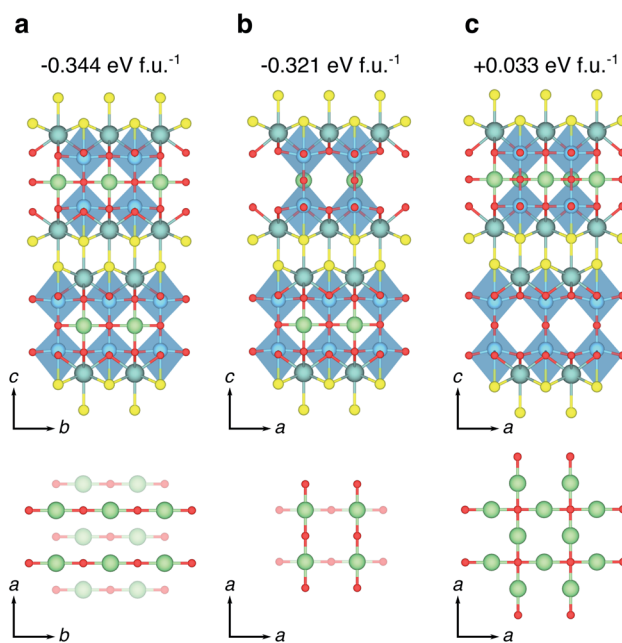


Fig. 7 High-symmetry Li orderings at $x = 1.0$ in $\text{Li}_x\text{Y}_2\text{Ti}_2\text{S}_2\text{O}_5$. (a) The ground state orthorhombic phase with Li-ions stacked AB, all forming bonds to O2 ions along the b direction. The lattice parameters of this structure are reported in Table 1. (b) A low-energy tetragonal phase obtained from an AA stacking of Li-ions, with Li on one plane forming bonds to O2 ions along the a direction, and Li on the next plane forming bonds to O2 ions along the b direction. (c) A high-energy tetragonal phase obtained from Li ions filling all sites on the same 2D plane, with the next plane empty. The reported energies are formation energies, calculated relative to the endmembers at $x = 0$ and $x = 2$.



structure, 0.023 eV per formula unit (f.u.) above the ground state, is a tetragonal phase where Li ions are equally distributed between the two Li-rich layers in the unit cell, stacked AA (Fig. 7b). In each layer, the Li-ions are arranged forming chains of Li-O2 bonds, but the chains in neighbouring layers are perpendicular when the structure is viewed along the *c*-direction. The structure with the highest-energy is obtained by filling all Li sites within one layer, and leaving the next layer empty (Fig. 7c), resulting in a tetragonal phase.

Li ordering at $x = 1.5$ in $\text{Li}_x\text{Y}_2\text{Ti}_2\text{S}_2\text{O}_5$. Fig. 8 shows three low-energy orderings of Li ions in the structure at $x = 1.5$. Two are isoenergetic structures on the hull, whilst the third structure is higher in energy by 3 meV per f.u. (Fig. 8a–c). All the structures are tetragonal, and all show the same arrangement of Li-ions within each Ti–O–S slab, where half the Li-ions have two Li neighbours and half have four. The difference in structure arises from the stacking of Li-ions in adjacent layers, but the contribution from this effect is clearly very small due to the similar energies of the structures.

Changing geometry of Li during lithiation. As the level of lithium within the structure increases, the geometry of the individual Li-ions changes. Under dilute conditions ($x = 0.125$ in $\text{Li}_x\text{Y}_2\text{Ti}_2\text{S}_2\text{O}_5$) the Li-ions are displaced out of the ‘windows’ into the W–R type 1 cavities (Fig. 9a) into a distorted ‘near-rectangular-planar’ geometry. However, at $x = 0.5$ the displacements into the cavities are suppressed, and the Li-ions adopt a rectangular-planar geometry. Similar geometry is also observed for $x = 1.0, 1.5$ and 2.0 (Fig. 9b). With increasing lithiation level, the *c* lattice parameter contracts, and the Li–O1 and Li–O2 bonds become closer in length. However, the rectangular-planar geometry is retained to full lithiation and the geometry never reaches ideal square-planar coordination; at $x = 2.0$, the Li–O1 bonds along the *c* direction are 2.00 Å, while the Li–O2 bonds along the *a* direction are 1.98 Å.

Changing shape of TiO_5S octahedra. Fig. 10 shows how the shape of the TiO_5S octahedra change as Li is intercalated. At $x = 0$, each TiO_5S octahedron is highly distorted with a short Ti–O2 bond, a long Ti–S bond and off-centring of the Ti ion. As intercalation progresses, the off-centring of the Ti reduces. The orthorhombic distortion at $x = 1$ results in shorter Ti–O1a

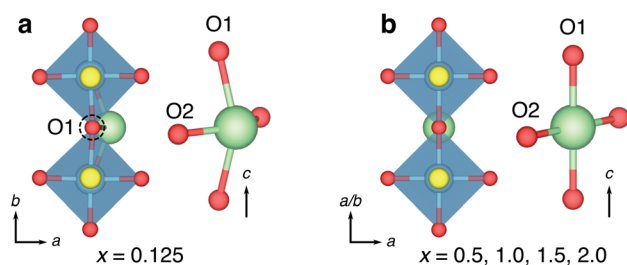


Fig. 9 Changing geometry of intercalated Li-ions with varying x in $\text{Li}_x\text{Y}_2\text{Ti}_2\text{S}_2\text{O}_5$. (a) Distorted ‘rectangular-near-planar’ Li^+ geometry under dilute conditions of $x = 0.125$. (b) Rectangular-planar geometry of Li^+ with increasing lithiation levels.

bonds (1.935 Å) and longer Ti–O1b bonds (1.953 Å) in the octahedron, a lengthening of the Ti–O2 bond, and a shortening of the Ti–S bond. At $x = 2$, the Ti–O1 and Ti–O2 bonds are 1.97 Å and 1.99 Å respectively and the Ti–S bonds are 2.42 Å. The shorter Ti–O2 and longer Ti–S bonds at $x = 2$ mean that the TiO_5S units are always distorted from octahedral symmetry, although all the O–Ti–O or O–Ti–S bond angles between adjacent vertices are 90°. The bonds lengths of the TiO_5S octahedra are reported in Table S3.†

Na^+ intercalation and mobility

A limiting factor in the development of batteries based upon intercalation of group I and II metals beyond lithium, is the slow ionic mobility of many of these species (*i.e.*, Na^+ , Mg^{2+}) in electrode or electrolyte materials.⁶⁴ Understanding the structural features of materials that give rise to high or low ionic mobility for ions of different size and charge will help guide the design of new materials.⁵⁹ In this section, we examine the intercalation and mobility of Na^+ in $\text{Y}_2\text{Ti}_2\text{S}_2\text{O}_5$, and compare its behaviour with that of Li^+ .

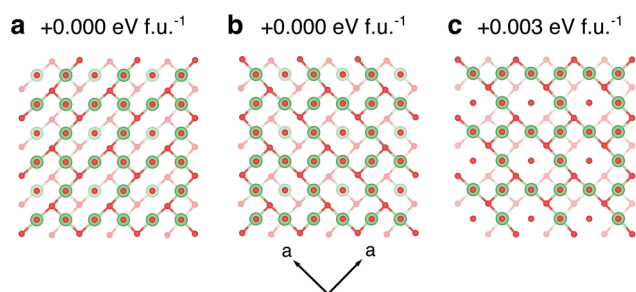


Fig. 8 Li orderings in the structure at $x = 1.5$. (a) and (b) are two symmetry-inequivalent ground-state orderings on the hull. The lattice parameters of (a) and (b) are similar, and the values for (a) are reported in Table 1. (c) A ordering of Li-ions that is +0.003 eV per f.u. above the hull. Solid and transparent units indicate atoms that are offset by one layer in the *c* direction.

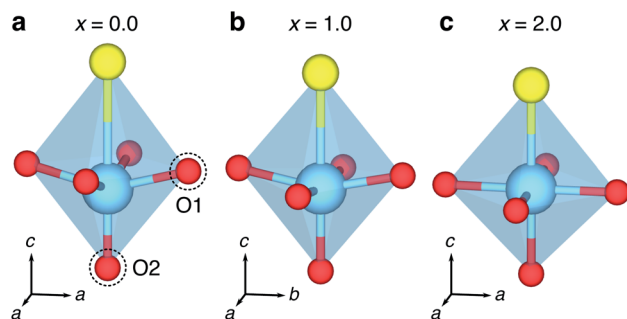


Fig. 10 Changing geometry of TiO_5S octahedra at different levels of lithiation. (a) Distorted TiO_5S units, with an off-centring of Ti along the *c* direction at $x = 0$, forming a short Ti–O2 bond, and a long Ti–S interatomic distance, and four equal Ti–O1 bonds. (b) Increasing lithiation to $x = 1.0$ reduces the distortion in the *c* direction and causes a orthorhombic distortion, resulting in extended Ti–O1 bonds along the *b* direction. (c) Full intercalation at $x = 2.0$ returns the structure to tetragonal and reduces the distortion along the *c* direction, and no off-centring of Ti. The corresponding Ti–O and Ti–S bond and interatomic distances are reported in Table S3.†



The intercalation of sodium ions can be achieved into two different positions within the $\text{Y}_2\text{Ti}_2\text{S}_2\text{O}_5$ lattice, depending on thermodynamic or kinetic reaction control.³⁴ At elevated temperatures (600 °C), thermodynamic control results in the insertion of sodium into the vacant 12-coordinate A sites in the type I cavities, producing $\alpha\text{-NaY}_2\text{Ti}_2\text{O}_5\text{S}_2$.³⁵ At or below 200 °C, sodium insertion produces $\beta\text{-NaY}_2\text{Ti}_2\text{O}_5\text{S}_2$ where the sodium cations insert into the interlayer space between the $[\text{Y}_2\text{S}_2]^{2+}$ rocksalt slabs, and adopt tetrahedral sites. If $\beta\text{-NaY}_2\text{Ti}_2\text{O}_5\text{S}_2$ is heated to 600 °C, $\alpha\text{-NaY}_2\text{Ti}_2\text{O}_5\text{S}_2$ is produced.

Fig. 11 shows the calculated geometry of a Na^+ ion in the central layer at a stoichiometry of $(\alpha)\text{-Na}_{0.125}\text{Y}_2\text{Ti}_2\text{S}_2\text{O}_5$. The Na^+ ion occupies the centre of the type I cavity, in a 12-coordinate environment to four O2 ions in the (001) plane with distances of 2.47 Å, and eight O1 ions with distances of 2.91 Å (Fig. 11a). The insertion of Na causes a small expansion of the unit cell in the (001) plane of 0.3%, retaining the tetragonal symmetry, and a small contraction of the c lattice parameter of -0.4%, consistent with observations from experiment.³⁵

There is one hopping pathway that Na can take, from a 12-coordinate site through a 'window' to an equivalent site in the next type I cavity. The path is shown in Fig. 11c, and the activation barrier, shown in Fig. 11d, is 1.7 eV. The transition state geometry is a four-fold rectangular-planar coordination, with two Na–O1 distances of 2.15 Å and two Na–O2 distances of 2.09 Å. The high activation barrier is a result of the large size of Na; in the 12-coordinate A site within the type I cavities the large Na

ion is stable and in a deep well on the potential energy surface, whereas the transition state represents a highly unstable geometry.

Our observation of a very high activation barrier for Na hopping between the type I cavity sites is consistent with the kinetic and thermodynamic control products α and $\beta\text{-NaY}_2\text{Ti}_2\text{O}_5\text{S}_2$ reported from experiment.³⁴ It can be expected that sodium intercalation will take place more easily within the rocksalt layers, where the activation barriers will be relatively low due to the weak electrostatic interaction between the mobile Na ion and S ions of the rocksalt framework. However the product of this favourable intercalation pathway, $\beta\text{-NaY}_2\text{Ti}_2\text{O}_5\text{S}_2$, is metastable with respect to the $\alpha\text{-NaY}_2\text{Ti}_2\text{O}_5\text{S}_2$ phase, which is thermodynamically preferred due to the stable position of the Na ions in 12 coordinate sites within the type I cavities.

It is interesting to note that K^+ ions, which have a larger radius than Na^+ , can be intercalated between the $[\text{Y}_2\text{S}_2]^{2+}$ rocksalt-type layers to form $\text{KY}_2\text{Ti}_2\text{S}_2\text{O}_5$, but cannot be inserted into the cages.³⁶ We hypothesise that K^+ may be thermodynamically stable located in the 12-coordinate site within the type I cavities, but its large size means that the ionic hop through the cage window requires an energy barrier that is too high to overcome, and incorporation between the rocksalt slabs is always the observed reaction pathway. Between the layers, K^+ ions adopt 8-fold coordinated rectangular cuboidal geometry, in contrast to the tetrahedral geometry observed for Na^+ ions in $\beta\text{-NaY}_2\text{Ti}_2\text{S}_2\text{O}_5$.

Our calculations indicate that the intercalation of Na and other large alkali or alkaline earth metal ions will be very challenging in materials composed of the building blocks of W–R phases.

Mg intercalation and mobility

The mobility of divalent Mg^{2+} within anhydrous crystalline structures is very limited, which represents a stumbling block for the development of batteries based upon Mg^{2+} intercalation chemistry.⁶⁴ Typically, mobility is higher within sulphides than oxides, and indeed there are only a handful of oxide materials that report reversible Mg^{2+} intercalation.^{65–67} Experimental results indicate that Mg^{2+} ions can be introduced into $\text{Y}_2\text{Ti}_2\text{S}_2\text{O}_5$ via a solid-state reaction route at 300 °C, to a stoichiometry of $\text{Mg}_{0.32}\text{Y}_2\text{Ti}_2\text{S}_2\text{O}_5$. Mg^{2+} ions were found to occupy 12-coordinated sites within the type I cavities.³⁵

Our DFT calculations identify two stable sites for Mg^{2+} in $\text{Y}_2\text{Ti}_2\text{S}_2\text{O}_5$. The first site, and the most stable, is the central site in the type I cavity. The Mg-ions forms four bonds to O2 ions in the ab plane of 2.15 Å and eight to O1 ions of 2.97 Å (Fig. 12a). The geometry may either be described as 12-coordinate, or four coordinate square-planar. There is a clear distortion to the host framework, with the O2 ions drawn in towards the Mg-ion, whilst the O1 ions are less significantly disturbed. A bond-valence sum calculation shows that the Mg-ion is highly under-bonded in this central site, with a value of ~ 1.42 .

The second site is a four-coordinate distorted rectangular-near-planar window site (Fig. 12b). The geometry is very similar to the position adopted by Li^+ , but the Mg-ion sits

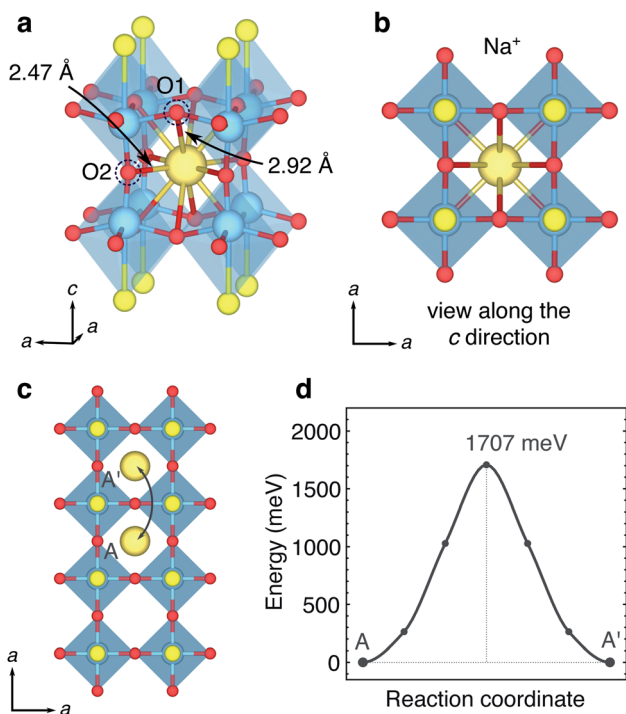


Fig. 11 Insertion and mobility of Na^+ in the central type I cavity layer. (a) The Na^+ ion sits in a 12-coordinated site in the centre of the 'cage'. (b) Structure viewed along the c direction. (c) Hopping path between 12 coordinated sites in adjacent 'cages'. (d) Activation barrier for the hopping pathway between $A \rightarrow A'$ in panel (c).



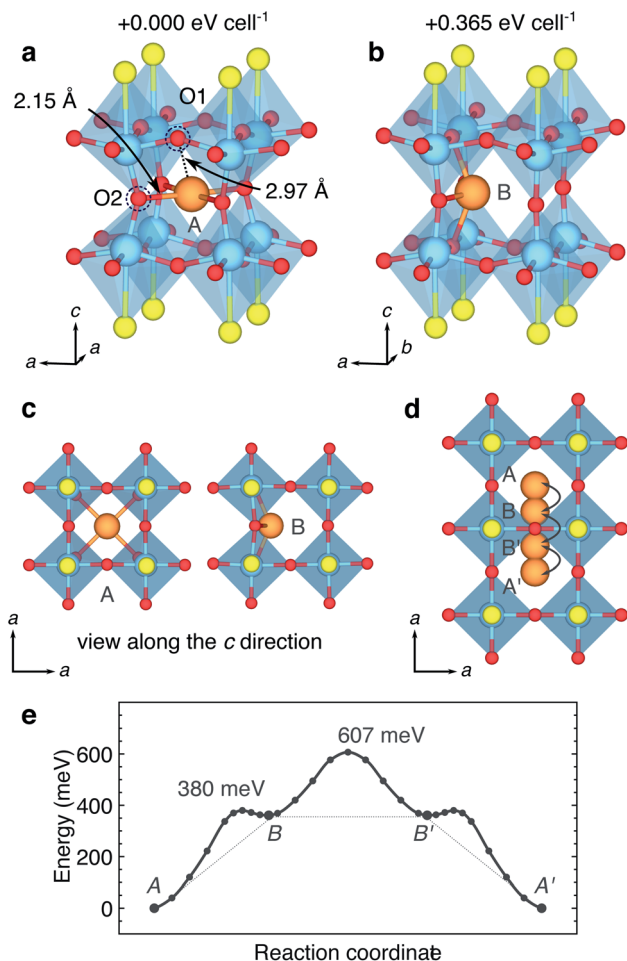


Fig. 12 Insertion and mobility of Mg^{2+} in the central type I cavity layer. (a) In the low-energy stable site A, Mg^{2+} ion sits in centre of the 'cage', either 12 or four-coordinate. (b) A metastable four-coordinate window site B. (c) Sites A and B viewed along the c direction. (d) Hopping path between central sites in adjacent 'cages'. (e) Energy profile for the migration from cage to cage.

further into the cage, and causes a greater distortion to the host framework than the Li ion. The window site is 0.365 eV higher in energy than the central site. There is no stable site for Mg^{2+} along the c direction, and a Mg-ion introduced into a 'horizontal' window at the top of the type I cavity migrates to the centre of the cage.

Fig. 12e shows the energy profile for Mg^{2+} moving from a central site in one cage, into the window sites, through the window to second window site and into the centre of the next cage. Hopping from the central site to the window site has a barrier of 0.380 eV. The window site is a very shallow local minimum on the potential energy surface. The hop through the window has a barrier of 0.607 eV with respect to the stable central site, and the remaining section of the migration profile is a reflection of the first section.

The activation barrier of 0.607 eV is relatively low for Mg^{2+} mobility in a crystalline material, and very low for mobility within an oxide framework.⁶⁴ Here, the Mg^{2+} moves within the central $[\text{Ti}_2\text{O}_5]^{2-}$ slabs and is not in contact with the S ions, so

the diffusion environment is comparable to that of an oxide. The difference in behaviour between Li and Mg-ions is a result of the different charge density of the two ions. Despite being of a similar size, the higher charge of the Mg-ion means it causes a strong distortion of the host lattice, and can be stabilised in the central cavity, rather than only at the window. The distortion of the host lattice by the Mg^{2+} suggests a reason for the low level of Mg^{2+} intercalation within the central cavities from experiment ($x = 0.32$), compared to Li^+ ($x = 2.0$) and Na^+ ($x = 1.0$). Once a Mg^{2+} ion is within a central cavity, the O2 of that cage will be drawn in towards the Mg^{2+} . This will tend to prevent other Mg-ions moving through and into neighbouring cages, since their potential energy surface will be disrupted. The distortion of the host framework by the Mg^{2+} effectively prevents the 'frustration' experienced by Li^+ , since the distortions act to stabilise the Mg^{2+} in a deeper well on the potential energy surface. As such, it is not possible to intercalate Mg^{2+} to a level that results in every other cage being occupied by a Mg-ion ($x = 0.5$).

The mobility of divalent Mg^{2+} within a bronze-type framework was recently reported by Johnson *et al.* in $\text{V}_4\text{Nb}_{18}\text{O}_{55}$,⁶⁶ which is structurally-related to the tetragonal tungsten bronzes, and has units similar to type I and II W-R-type cavities. Activation barriers of similar magnitude were reported for selected pathways and Mg-ions we found to occupy distorted square- or rectangular-planar insertion sites. Mg^{2+} intercalation in $\text{V}_4\text{Nb}_{18}\text{O}_{55}$ was limited to a low level. Taken together, these results and other similar reports^{68,69} indicate that Mg^{2+} mobility is possible within W-R-type frameworks under dilute conditions, but the high charge of Mg^{2+} induces distortions to the framework that yield low energy minima on the potential energy surface and limit intercalation to low levels.

Electronic structure of $\text{Y}_2\text{Ti}_2\text{S}_2\text{O}_5$

A limiting factor in electrode materials, as well as ionic conductivity, is the electronic transport. Materials with Wadsley–Roth-type structures typically display an insulator-to-metal transition at low levels of lithiation, due to delocalised electrons in the conduction band, which is composed of relatively diffuse Nb 4d orbitals.^{18,29,30,53,70} $\text{Y}_2\text{Ti}_2\text{S}_2\text{O}_5$ is a medium-gap semiconductor³³ with a bandgap of ~ 2 eV, and it has been applied as a photocatalyst for overall water-splitting under visible light.⁵² Upon intercalation of Li^+ ions, $\text{Li}_x\text{Y}_2\text{Ti}_2\text{S}_2\text{O}_5$ is reported to behave as a semiconductor at $x = 0.3$, with some degree of Curie contribution to the magnetic susceptibility, indicating the presence of localised $S = 1/2$ magnetic moments, attributed to localised electrons on Ti^{3+} ions. $\text{Y}_2\text{Ti}_2\text{S}_2\text{O}_5$ becomes metallic at $x > 1$, with a predominantly temperature-independent contribution to the magnetic susceptibility, indicative of Pauli paramagnetism.³⁷

Fig. 13 shows the electronic density of states for $\text{Y}_2\text{Ti}_2\text{S}_2\text{O}_5$, calculated using HSE06-D3. The bandgaps calculated with other functionals are presented in Table S1.† The valence band is mainly composed of occupied O 2p and S 3p states, while the conduction band is predominantly composed of unoccupied Ti 3d and Y 5d states (Fig. 13a). The Y 5d states lie approximately



4 eV above the conduction band minimum (CBM) and mainly overlap with S 3p states (Fig. 13b). The unoccupied Ti 3d states in the conduction band show a characteristic octahedral crystal field splitting, with a t_{2g} band of d_{xy} , d_{xz} and d_{yz} lying below the e_g band of $d_{x^2-y^2}$ and d_{z^2} orbitals (Fig. 13c). The distortion from regular octahedral symmetry disrupts the crystal field, lowering the energy of the d_{z^2} orbital slightly so that it overlaps with the t_{2g} band. Within the t_{2g} band, the d_{xy} orbital is unique, while the d_{xz} and d_{yz} are equivalent by symmetry. There is almost no contribution from Ti 3d states to the valence band maximum (VBM), which is composed of S 3p states only (Fig. 13c and d). The absence of hybridisation between Ti 3d and S 3p orbitals is consistent with the long Ti-S distance of ~ 2.87 Å. There is a small contribution from the Ti 3d states to the lower edge of the valence band at approximately -4 eV (indicated by the grey area). In this region, a sharp peak from the Ti $3d_{z^2}$ aligns with

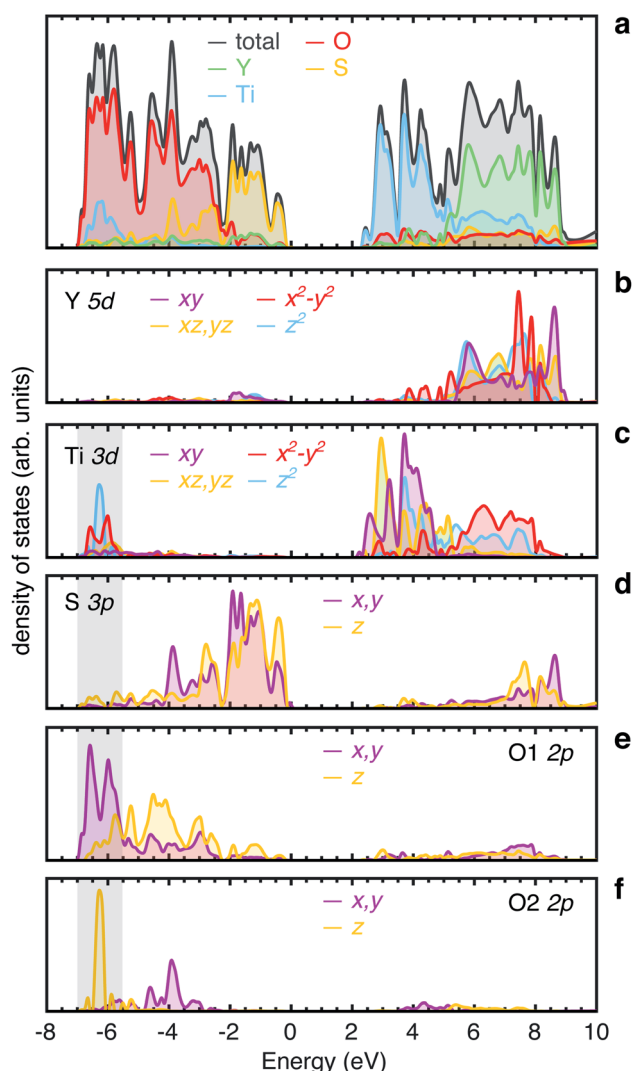


Fig. 13 Electronic density of states for $Y_2Ti_2S_2O_5$ calculated using HSE06-D3. (a) Total density of states and contribution from different atom-types. (b)–(f) Partial density of states, projected onto valence shells for individual Y, Ti, S, O1 and O2 atoms respectively, including orbital contributions. The grey area at -6 eV highlights the energy region in which the Ti 3d and O 2p contributions overlap.

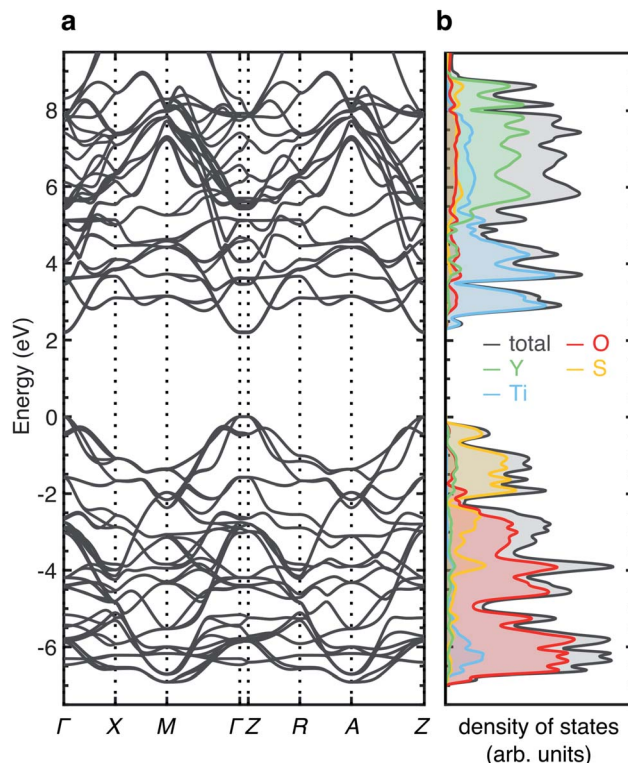


Fig. 14 Electronic band structure of $Y_2Ti_2S_2O_5$ calculated using HSE06-D3. (a) Electronic band structure. (b) Total and partial electronic density of states.

a highly localised band from the O2 $2p_z$, consistent with the orientational overlap expected from these two orbitals (Fig. 13c and f). The Ti $3d_{x^2-y^2}$ band shows two small peaks at approximately -6 eV and -6.5 eV at the bottom of the valence band, which align with the O1 $2p_x$ and $2p_y$ orbitals, indicating Ti–O covalent interactions (Fig. 13c and e). The calculated bandgap from HSE06-D3 is 2.19 eV.

A previous report of the electronic density of states using the PBE functional showed a very different character, with the valence band maximum composed of overlapping S 3p and O 2p states.⁵² The overlapping contributions were advanced as evidence for hybridisation between S 3p and O 2p states. However, overlapping peaks in the electronic density of states do not necessarily indicate orbital hybridisation, since orbitals may overlap in energy, but not in space. In the present case, the O^{2-} and S^{2-} anions form separate sub-bands of the valence band, and our results indicate that there is negligible orbital overlap.

Fig. 14 shows the electronic band structure of $Y_2Ti_2S_2O_5$ calculated using HSE06-D3. The VBM and CBM regions both show highly parabolic bands, indicating high electron and hole mobility. The band structure shows a direct bandgap at the Γ and Z points in the Brillouin zone.

Physical origin of the orthorhombic distortion at $x = 1$ in $Li_xY_2Ti_2S_2O_5$

The orthorhombic distortion at $x = 1$ (*i.e.*, half-lithiation) is the primary structural change in the system, causing a clear drop in



the voltage curve, and is therefore an important feature to understand. Hyett *et al.* propose that the orthorhombic distortion is electronically-driven by lifting the degeneracy of the Ti $3d_{xz}$ and $3d_{yz}$ orbitals.³⁷ The results presented here show that Li-ions are highly mobile and will fill sites in a correlated fashion during lithiation of $Y_2Ti_2S_2O_5$. This raises the possibility that orthorhombic distortion is a steric effect, initiated by a Li-ion ordering arising from correlated Li-dynamics, rather than arising from an electronic band-filling effect.

In Li-ion conductors under dilute conditions, Li-ion mobility can be well described by a single-ion hopping mechanism and in the absence of an external potential, self-diffusion will take place through a random-walk.^{71,72} However, at non-dilute concentrations significant Li-Li interactions produce pronounced deviations from the random-walk behaviour that occurs in the dilute limit. Li^+ motion becomes highly correlated, and the correlation depends on a range of factors including the concentration of mobile species, interactions between those species and the host lattice geometry.⁵⁰ Depending on these factors, the correlation effects may give rise to Li-orderings at certain states of charge.

The correlated behaviour of mobile particles in solids can be examined using lattice-gas Monte-Carlo (MC) simulations. The network of sites that Li-ion occupy in $Li_xY_2Ti_2S_2O_5$ can be described as a square lattice, and a model was constructed to represent this network. Alternating sites were labelled A and B, and each site was connected to neighbours of opposite type only, representing the possible hops Li ions can make from window site to window site along path 2 (Fig. 15a). Lattice-gas MC simulations were run at different levels of lithiation, and an 'order-parameter' was computed, taking the absolute difference in site occupation for A and B sites for each simulation. An order parameter of 0 indicates an even population of the two types of sites whereas an order parameter of 1 indicates all A sites occupied with B unoccupied, or all B sites occupied

with A unoccupied. We note that distortions of the Li-ions into the 'windows' under dilute conditions mean that the Li-ion site network is not perfectly described by a square lattice in this low lithium level. However, a square lattice describes the site network in the region of interest ($x > 0.5$) that we focus upon here.

Fig. 15b shows the order parameter for different levels of Li concentration, calculated at different values of nearest-neighbour interaction (n). At $x = 1$ ($LiY_2Ti_2S_2O_5$), the order parameter is a maximum, and is equal to 1 when $n > 1$, showing that Li-ion order in chains along one $\langle 100 \rangle$ direction. These results are consistent with previous lattice-gas MC simulations of mobile particles on a square lattice.^{73,74} The lattice-gas MC model is based purely upon nearest-neighbour interactions and omits structural distortions and electronic effects. The results therefore confirm that in the absence of an orthorhombic distortion and band filling, Li-ions will order in $LiY_2Ti_2S_2O_5$ forming chains along the b direction.

Secondly, we examine the Li-ordered structure at $x = 1$ under modified band-filling conditions. Two electrons were removed from the Ti 3d orbitals in the unit cell of $LiY_2Ti_2S_2O_5$, and charge neutrality was recovered by applying a uniform background screening. From a tetragonal starting cell, the structure was re-optimised. The final structure displays an orthorhombic distortion, with (001)-plane lattice parameters of $a = 3.681$ Å and $b = 3.796$ Å, a difference of 0.115 Å. In comparison, the charge-neutral cell lattice parameters are $a = 3.841$ Å and $b = 3.911$ Å, a difference of 0.070 Å. Fig. 16a shows the electronic density for the orthorhombically-distorted structure with two electrons removed. The sterically-induced orthorhombic distortion of the structure lowers the energy of the Ti $3d_{yz}$ orbital, breaking the degeneracy with the Ti $3d_{xz}$ orbital, despite the Ti $3d_{yz}$ being unoccupied.

This result demonstrates that in the presence of Li-ion chains along the b axis and the absence of band-filling, the orthorhombic distortion is observed. Therefore, we propose that the origin of the orthorhombic distortion is the Li-ion ordering, rather than band-filling effects. The Li-ion ordering arises due to electrostatic repulsion of the Li-ions at half-filling on the square lattice of sites. We note that the region in which the orthorhombic distortion occurs ($0.66 < x < 1.52$) in $Li_xY_2Ti_2S_2O_5$, as reported by Hyett *et al.*,³⁷ corresponds very closely with the region in which the order parameter has an appreciable value from our lattice-gas Monte-Carlo model ($0.5 < x < 1.5$). This further supports the idea that the Li-ion ordering is the driver for the orthorhombic distortion.

Finally, we analyse the electronic density of states for $LiY_2Ti_2S_2O_5$ in a charge-neutral cell, under normal band-filling conditions (Fig. 16b). The system is metallic, consistent with experimental magnetic susceptibility measurements,³⁷ with electrons filling the Ti 3d orbitals at the bottom of the conduction band. The degeneracy of the Ti $3d_{xz}$ and Ti $3d_{yz}$ is indeed lifted, with the Ti $3d_{yz}$ orbitals stabilised over the Ti $3d_{xz}$ orbitals (Fig. 16b), consistent with the results of Hyett *et al.*³⁷ The Ti $3d_{yz}$ now overlaps with the Ti $3d_{xy}$ orbital, and the Fermi energy crosses both. The orthorhombic distortion is less for the neutral cell (0.070 Å) than the cell with two electrons removed

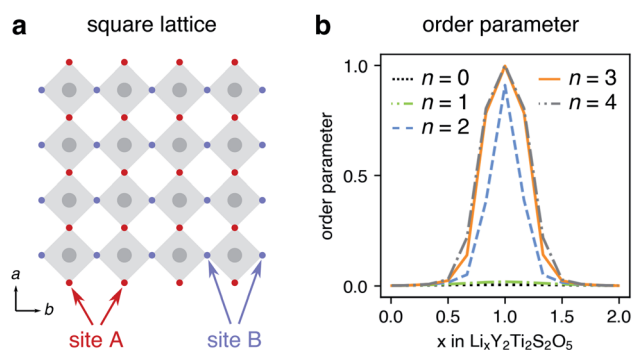


Fig. 15 Correlated Li-ion ordering in $Li_xY_2Ti_2S_2O_5$ from lattice-gas Monte-Carlo simulations. (a) A 2D square lattice of sites, representing the network of sites that Li-ions can occupy in $Li_xY_2Ti_2S_2O_5$. Alternate sites are labelled A and B, and each site is connected to sites of an opposite label only. Grey shaded squares indicate the TiO_5S octahedra, viewed along the c direction. The b axis indicates the direction in which chains of Li-ions are formed. (b) The calculated 'order-parameter' with varying lattice occupation (i.e., x in $Li_xY_2Ti_2S_2O_5$). The order parameter is calculated as the absolute difference in site occupation for A and B sites.



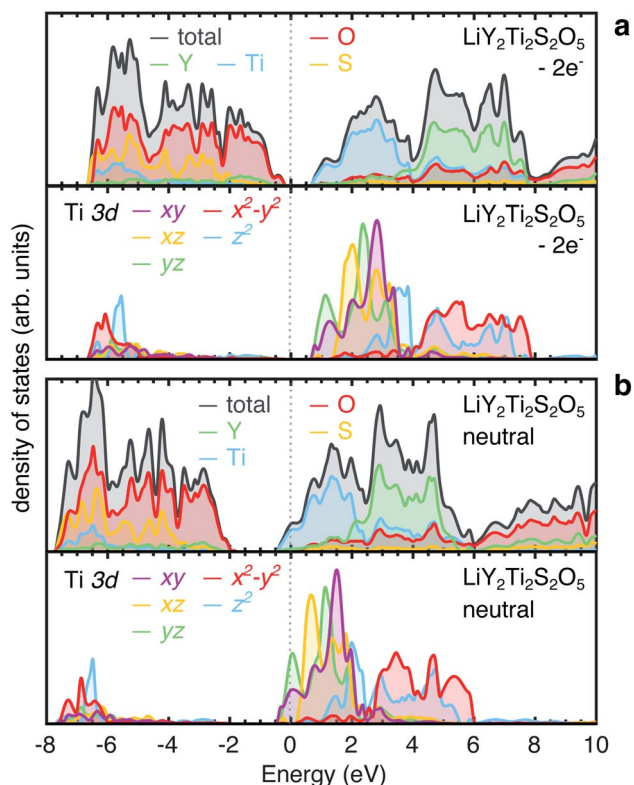


Fig. 16 Electronic density of states for $\text{LiY}_2\text{Ti}_2\text{S}_2\text{O}_5$ calculated using PBEsol under varying band-filling conditions. (a) Total and atom-projected electronic density of states for the low-energy ordering of Li-ions in $\text{LiY}_2\text{Ti}_2\text{S}_2\text{O}_5$ (Fig. 7a), with two electrons removed from the unit cell, and a background screening applied to compensate the removed electrons. (b) Total and atom-projected electronic density of states for the low-energy ordering of Li-ions in $\text{LiY}_2\text{Ti}_2\text{S}_2\text{O}_5$, in a charge-neutral cell, under normal band-filling conditions.

(0.115 Å), implying that the band-filling acts to lower the effect of the orthorhombic distortion, by partial filling of the Ti $3d_{xy}$ orbital (which causes isotropic expansion in the (001) plane), rather than filling the Ti $3d_{yz}$ only.

Discussion

$\text{Y}_2\text{Ti}_2\text{S}_2\text{O}_5$ is a model system within which to understand the mechanisms of Li^+ ion diffusion in Wadsley–Roth and related bronze-type structures. Wadsley–Roth phases have complex crystal structures with a variety of cavity shapes into which Li^+ can be accommodated. They show disordered occupation of cations in $[\text{MO}_6]$ octahedra, predicted to affect local Li^+ -hopping energies,^{30,53} and in some cases fractional occupation of $[\text{MO}_4]$ tetrahedra within type III and VI cavities.²¹ Li^+ diffusion is predominantly 1D down the block columns in W–R phases. However, movement of Li^+ ions perpendicular to the column direction between type I cavities and higher activation barriers for sites for Li^+ ions hopping into ‘pocket’ at $n \times m$ block edges introduces complexity and additional dimensionality to the potential energy surface for Li^+ mobility.²⁹ In contrast, the movement of Li^+ is entirely 2D within $\text{Y}_2\text{Ti}_2\text{S}_2\text{O}_5$, and the type I cavities are homogeneous across the entire structure, greatly

simplifying the potential energy surface for Li^+ -hopping. Insights into structural properties that activate high Li^+ mobility in the simple 2D structure of $\text{Y}_2\text{Ti}_2\text{S}_2\text{O}_5$ may provide a basis for understanding the more complex case of Wadsley–Roth type structures.

The high-rate performance of $\text{Y}_2\text{Ti}_2\text{S}_2\text{O}_5$ as an Li-ion anode material³⁸ can be attributed to the low activation barriers for Li^+ hopping between sites. The origin of the very low barriers under dilute conditions in $\text{Y}_2\text{Ti}_2\text{S}_2\text{O}_5$ is the unusual four-coordinate distorted rectangular-near-planar type insertion geometry. This geometry is ‘frustrated’ or unstable with respect to more favourable coordination environments such as octahedral or tetrahedral. Similar geometry is also observed in W–R-type phases, when Li-ion occupy type I cavities. The Li-ions are too small to be stable in the central 12 coordinate A site within the cavities and instead reside by the edge, in ‘frustrated’ window sites.

Our results reveal the importance of the size and shape of the type I cavity windows on the Li-ion insertion geometry, and by extension the shape of the potential energy surface for Li-hopping and the diffusion rate. In the case of a large window (with a width and height of ~ 4 Å or greater), it would be expected that the Li-ion would reside flush in line with the O1 ion when the structure is viewed along the c direction. Each window would therefore constitute a single insertion site, and Li-ion hopping would take place by direct hops between windows, the network of sites defined by a square lattice (Fig. 17a).

However, in $\text{Y}_2\text{Ti}_2\text{S}_2\text{O}_5$ the type I cavities are tetragonally extended and as such, the windows are tall and narrow. The Li-ions cannot reside flush in the windows and are squeezed slightly into the cavities. The position of Li^+ in an approximately square-planar window site, identified from neutron diffraction experiments,³⁷ is revealed to be the average of two ‘symmetry-broken’ stable positions either side of the window (at 0 K). This displacement into the cavities has two effects on Li-ion hopping. Firstly, the network of stable sites is modified, since there are equilibrium positions either side of the window. The network is now represented by a truncated square tiling (Fig. 17b). Secondly, the Li-ions are destabilised (or ‘frustrated’) further, and raised higher on the potential energy surface by some value ΔE_{dist} (Fig. 17c).

Li-ion hopping can now take place *via* two small steps; a rattling through the window, which has a very low barrier (determined by the magnitude of displacement into the cage), and a hop along the edge of the cavity to another window site. Since the Li-ion has been raised on the potential energy surface, this second hop is likely to have a lower activation barrier than the direct hop between window sites (assuming the energy of the transition state remains approximately constant). The displacement into the cavity by the narrow window size therefore has the effect of smoothing the potential energy surface, and giving rise to fast Li-ion diffusion. This effect is likely to be general to Li-ion diffusion within the type I cavities of W–R phases; the window size affects the stability of the insertion site and the magnitude of the activation barrier to Li-ion hopping. We speculate that as the window size is decreased further, the activation barrier for hopping through the window will increase,



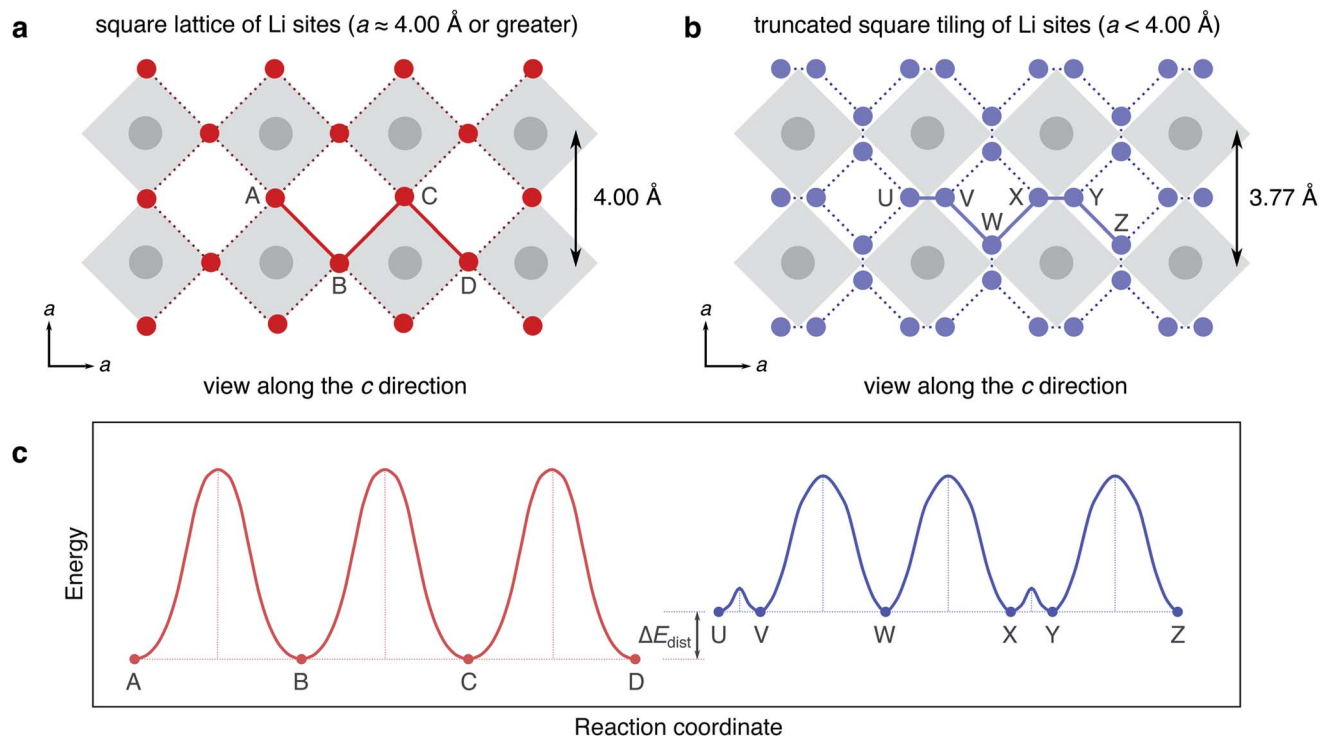


Fig. 17 Effects of lattice parameter and 'window' size on the potential energy surface for Li^+ hopping in type I cavities. The grey shaded areas represent the octahedra of the Ti^{4+} ions, red and blue circles indicate the sites that Li can occupy, and the solid red and blue lines indicate Li hopping pathways, while dotted lines indicate the network of possible diffusion pathways. (a) Illustration of Li-hopping on a square lattice with $a = 4 \text{ \AA}$. Stable sites for Li^+ ions are in symmetric square planar sites due to the ideal window size. (b) Illustration of Li-hopping on a compressed lattice with $a = 3.77 \text{ \AA}$. The smaller window size destabilises the symmetric square-planar geometry, causing a distortion into the cage lowering the symmetry of the Li^+ site network. The square-planar sites, in line with O-ions when the structure is viewed along the c direction, are now transition states for Li-ion 'rattling' between stable sites. (c) Illustration of the potential energy surface for Li^+ ions hopping on the two lattices. ΔE_{dist} is the destabilisation of the Li^+ sites when pushed into the distorted square-planar geometry due to the small window size.

but the barrier for hopping to a new window site will decrease. The results therefore imply that there is some 'ideal' window size to achieve the fastest Li-ion diffusion within type I cavities, that will result in a maximum 'smoothing' of the potential energy surface for Li-ion hopping. To test this hypothesis, the varying window size for isostructural materials within the $\text{Ln}_2\text{-Ti}_2\text{S}_2\text{O}_5$ series ($\text{Ln} = \text{Nd, Sm, Gd, Tb, Dy, Ho, Er}$)³³ could be exploited, and the Li-ion diffusivity could be compared between the materials. In W-R frameworks the presence of type II and other cavities complicates the picture for Li-ion diffusion, as do effects such as framework cation off-centring, and cation disorder.

At non-dilute Li-concentrations ($x > 0.5$ in $\text{Li}_x\text{Y}_2\text{Ti}_2\text{S}_2\text{O}_5$), Li-Li repulsion pushes the Li-ions into an undistorted rectangular planar geometry flush in the 'windows' (Fig. 9). The Li-ion hops will now be described by a square lattice of sites. It is expected that activation barriers will remain low, since the rectangular-planar geometry is still 'frustrated'. The diffusion rate remains high, as is apparent from the experimental discharge rate curves.³⁸ In corner-sharing-only octahedral frameworks such as ReO_3 , the frustrated geometry of Li is lost on increasing levels of lithiation. The presence of the rocksalt $[\text{Y}_2\text{S}_2]^{+}$ slabs provides rigidity to the type I cavity framework, and the octahedral units do not experience correlated rotations and

distortions as Li intercalation levels are increased. The rocksalt slabs therefore have a similar effect to the shear planes in W-R phases, but without reducing the Li-ion diffusion dimensionality to 1D.

As discussed above, in fast Li-ion conductors at non-dilute conditions, Li-ion diffusion will be dominated by Li-Li interactions, resulting in highly correlated ionic motions. This effect is expected to be prevalent in Li-ion conductors based on W-R motifs. Recently, Griffith and Grey have applied ^7Li pulsed-field-gradient nuclear-magnetic-resonance (PFG-NMR) spectroscopy to probe Li^+ diffusion in $\text{Nb}_{18}\text{W}_8\text{O}_{69}$ at room temperature (298 K).¹⁹ The technique is generally not suitable for measuring diffusion in battery electrodes, since Li^+ mobility is too slow in most electrode materials. However, since the diffusion coefficients for Li^+ in Wadsley-Roth type materials are orders of magnitude greater than in many battery electrode materials, PFG-NMR spectroscopy measurements are possible. These experiments indicated correlated Li^+ diffusion characteristics. However, due to the resolution of the data, and the complex Li^+ diffusion in 3 directions within the $2 \text{ nm} \times 2 \text{ nm}$ width 5×5 blocks, a precise determination of the correlation effects was not possible. The relatively simple 2D diffusion plane of $\text{Y}_2\text{Ti}_2\text{S}_2\text{O}_5$, and the high-rate discharge performance make it a model material for investigating correlated Li^+ diffusion using



experimental techniques. The effects of correlated diffusion on simple square networks of sites are well known from lattice-gas Monte-Carlo simulations,^{73–76} and could be examined in greater detail in $\text{Y}_2\text{Ti}_2\text{S}_2\text{O}_5$ with classical or *ab initio* molecular dynamics simulations of Li-ion diffusion.

The stable orderings at $x = 1$ and $x = 1.5$ are expected to cause a significant drop in the diffusion coefficient, since Li-ion hopping out of these stable orderings will have to overcome Li–Li repulsion effects. The stable orderings arise from Li–Li repulsion effects; if all the sites on a square lattice are similar in energy, orderings will appear at the half-filled lattice to maximise distance between mobile cations. One strategy to inhibit these orderings would be to disrupt the stability of the network of sites through doping or chemical substitution of ions of different size into the framework. For example, substitution of Nb in place of Ti, or Se in place of S may modify the site stability network.

Although our study on $\text{Y}_2\text{Ti}_2\text{S}_2\text{O}_5$ is dedicated to understand its intercalation behaviour, analysis of the calculated electronic density of states has also allowed us to investigate the structural–chemical features that enable the same material to be an efficient photocatalyst. The density of states results presented in Fig. 13, calculated using HSE06, clearly show that the VBM arises from S 3p states and the CBM is composed of Ti 3d states. Photo-generated electrons will therefore be located in the Ti 3d band, while holes will be located in the S 3p band. Although we describe the structure of the material as based on type I cavities formed by $[\text{TiO}_5\text{S}]$ octahedra, the highly distorted nature of the Ti octahedra, mean that the Ti–S distance is $>2.8 \text{ \AA}$, longer than typical Ti–S bonds in other crystalline materials such as TiS_2 ($\sim 2.4 \text{ \AA}$).⁷⁷ The spatial overlap between Ti 3d and S 3p orbitals is therefore expected to be small.

Carrier recombination is a crucial mechanism in determining the efficiency of water-splitting photocatalysts. Materials displaying long carrier lifetimes show high efficiency, since photogenerated electron–hole pairs are able to migrate to surfaces to perform work. Various strategies are employed to reduce carrier recombination, one of which is the design of heterostructural interfaces comprised of two materials with tuned band positions for efficient extraction and separation of photogenerated electron–hole pairs into each material.⁷⁸ Indeed, it has been suggested that a single material is unlikely to mediate the entire sequence of charge and mass transport as well as energy conversion processes necessary for photocatalytic water-splitting.⁷⁹ However, if a single crystalline material has a structure in which subsets of cations and anions are (i) physically separated in space and (ii) have band energies that form the VBM and CBM, combined with the other band structure properties required for photocatalytic water-splitting, then the entire sequence can be possible within one compound.⁸⁰

Layered ternary or quaternary oxychalcogenide or oxypnictide compounds such as $\text{Ln}_2\text{Ti}_2\text{S}_2\text{O}_5$,^{31–33} BiCuSeO ⁸¹ and LaFeAsO ⁸² contain structural sub-units that make distinct contributions to the band edges, and thus combine structural and electronic features that yield the separation of electronic states in both energy and space. We speculate that this mechanism may contribute to the excellent photocatalytic activity of

$\text{Y}_2\text{Ti}_2\text{S}_2\text{O}_5$ and $\text{Sm}_2\text{Ti}_2\text{S}_2\text{O}_5$.^{52,83} With advances in the design⁸⁴ and modular synthesis of layered mixed-anion semiconductors,⁸⁵ it may be possible to employ this strategy for the design of improved photocatalysts that efficiently separate charges and maximise carrier lifetimes.

Conclusions

In this work we have investigated the structure and Li^+ , Na^+ and Mg^{2+} intercalation properties of the high-rate Li-ion anode materials $\text{Y}_2\text{Ti}_2\text{S}_2\text{O}_5$, using DFT calculations and lattice-gas Monte Carlo simulations. $\text{Y}_2\text{Ti}_2\text{S}_2\text{O}_5$ has an unusual layered Ruddlesden–Popper-type structure, with an empty central plane formed of TiO_5S octahedra, that relate to the type I ‘empty-perovskite’ cavities within structural units that form Wadsley–Roth crystallographic shear phases.

Li^+ , Na^+ and Mg^{2+} ions can be intercalated on this central plane. DFT calculations show that Li-ions adopt a four-coordinate distorted rectangular-near-planar geometry, near the windows of the cavities and ‘rattle’ between to sites either side of the window with activation barriers of 20 meV. Li-ion hopping barriers between adjacent windows are 64 meV under dilute conditions. The low activation barriers relate to the size and shape of the cavities; the tall narrow size of the windows destabilises the Li-ions, pushing them into the type I cavities and reducing the magnitude of the activation barrier they must overcome to move, resulting in a very flat potential energy surface. Since Li-diffusion happens very easily, Li–Li repulsion governs Li-ordering during the intercalation process. Lattice-gas Monte-Carlo simulations show that Li-ions form chains along the *b*-axis at $x = 1$, driven Li–Li repulsion. This ordering, an effect of correlated particle interactions, drives an orthorhombic distortion of the structure. The rocksalt-type slabs Y–S provide rigidity to the framework, such that no correlated rotations of the ‘empty-perovskite’ framework occur on Li intercalation.

Na^+ hopping barriers are high, which is attributed to the large size and high stability of Na^+ within the central 12-coordinated sites of the cavities. The results suggest that W–R-type materials are not good Na-ion conductors. Mg-ions move with single-ion hopping barriers of 0.604 eV, but strong host framework distortions hinder their mobility and limit intercalation to low levels.

Despite focusing on intercalation properties in $\text{Y}_2\text{Ti}_2\text{S}_2\text{O}_5$, we have shown that the localisation of valence and conduction band edges in occurs in spatially separated sub-units of the structure. This is likely to decrease the recombination rate of photo-generated charge-carriers, and contribute to the high photocatalytic activity reported for $\text{Y}_2\text{Ti}_2\text{S}_2\text{O}_5$ (ref. 52) and isostructural compounds.⁸³ Similar features are expected to occur in other layered ternary or quaternary oxychalcogenides and oxypnictide compounds.

The results presented here for $\text{Y}_2\text{Ti}_2\text{S}_2\text{O}_5$ provide insights into the structural origin of fast Li-ion diffusion in materials related to the Wadsley–Roth phases, and will help guide the development of high-power electrode and electrolyte materials.



Conflicts of interest

There are no conflicts to declare.

Acknowledgements

K. M. thanks Megan M. Butala and Can P. Koçer for valuable discussions. The authors thank the EPSRC for funding the JUICED project (EP/R023662/1) and acknowledge membership of the UK's HEC Materials Chemistry Consortium, which is funded by EPSRC (EP/L000202, EP/R029431). This work used computational resources provided by the ARCHER UK National Supercomputing Service (<http://www.archer.ac.uk>) and the UK Materials and Molecular Modelling Hub (MMM Hub), which is partially funded by EPSRC (EP/P020194). The authors acknowledge the use of the UCL Grace and Kathleen High Performance Computing Facilities (Grace@UCL), (Kathleen@UCL), and associated support services, in the completion of this work.

References

- 1 Y. Liu, Y. Zhu and Y. Cui, *Nat. Energy*, 2019, **4**, 540–550.
- 2 P. Bruce, B. Scrosati and J.-M. Tarascon, *Angew. Chem., Int. Ed.*, 2008, **47**, 2930–2946.
- 3 A. Lennon, Y. Jiang, C. Hall, D. Lau, N. Song, P. Burr, C. P. Grey and K. J. Griffith, *MRS Energy Sustain.*, 2019, **6**, E2.
- 4 S. Megahed and B. Scrosati, *J. Power Sources*, 1994, **51**, 79–104.
- 5 M. Winter, B. Barnett and K. Xu, *Chem. Rev.*, 2018, **118**, 11433–11456.
- 6 P. Arora, R. E. White and M. Doyle, *J. Electrochem. Soc.*, 1998, **145**, 3647–3667.
- 7 J. Vetter, P. Novák, M. Wagner, C. Veit, K.-C. Möller, J. Besenhard, M. Winter, M. Wohlfahrt-Mehrens, C. Vogler and A. Hammouche, *J. Power Sources*, 2005, **147**, 269–281.
- 8 M. V. Reddy, G. V. Subba Rao and B. V. R. Chowdari, *Chem. Rev.*, 2013, **113**, 5364–5457.
- 9 T. Ohzuku, A. Ueda and N. Yamamoto, *J. Electrochem. Soc.*, 1995, **142**, 1431–1435.
- 10 K. Zaghib, M. Simoneau, M. Armand and M. Gauthier, *J. Power Sources*, 1999, **81–82**, 300–305.
- 11 X. Sun, P. V. Radovanovic and B. Cui, *New J. Chem.*, 2015, **39**, 38–63.
- 12 L. Sun, J. Wang, K. Jiang and S. Fan, *J. Power Sources*, 2014, **248**, 265–272.
- 13 V. Augustyn, J. Come, M. A. Lowe, J. W. Kim, P.-L. Taberna, S. H. Tolbert, H. D. Abruña, P. Simon and B. Dunn, *Nat. Mater.*, 2013, **12**, 518–522.
- 14 K. J. Griffith, A. C. Forse, J. M. Griffin and C. P. Grey, *J. Am. Chem. Soc.*, 2016, **138**, 8888–8899.
- 15 D. Chen, J.-H. Wang, T.-F. Chou, B. Zhao, M. A. El-Sayed and M. Liu, *J. Am. Chem. Soc.*, 2017, **139**, 7071–7081.
- 16 J.-T. Han, Y.-H. Huang and J. B. Goodenough, *Chem. Mater.*, 2011, **23**, 2027–2029.
- 17 K. J. Griffith, K. M. Wiaderek, G. Cibir, L. E. Marbella and C. P. Grey, *Nature*, 2018, **559**, 556–563.
- 18 M. B. Preefer, M. Saber, Q. Wei, N. H. Bashian, J. D. Bocarsly, W. Zhang, G. Lee, J. Milam-Guerrero, E. S. Howard, R. C. Vincent, B. C. Melot, A. Van der Ven, R. Seshadri and B. S. Dunn, *Chem. Mater.*, 2020, **32**, 4553–4563.
- 19 K. J. Griffith and C. P. Grey, *Chem. Mater.*, 2020, **32**, 3860–3868.
- 20 S. Andersson and A. D. Wadsley, *Nature*, 1966, **211**, 581–583.
- 21 R. J. Cava, D. W. Murphy and S. M. Zahurak, *J. Electrochem. Soc.*, 1983, **130**, 2345–2351.
- 22 J. P. Parras, A. R. Genreith-Schriever, H. Zhang, M. T. Elm, T. Norby and R. A. De Souza, *Phys. Chem. Chem. Phys.*, 2018, **20**, 8008–8015.
- 23 R. Cava, A. Santoro, D. Murphy, S. Zahurak and R. Roth, *Solid State Ionics*, 1981, **5**, 323–326.
- 24 R. Cava, A. Santoro, D. Murphy, S. Zahurak and R. Roth, *J. Solid State Chem.*, 1982, **42**, 251–262.
- 25 N. H. Bashian, S. Zhou, M. Zuba, A. M. Ganose, J. W. Stiles, A. Ee, D. S. Ashby, D. O. Scanlon, L. F. J. Piper, B. Dunn and B. C. Melot, *ACS Energy Lett.*, 2018, **3**, 2513–2519.
- 26 K. Qi, J. Wei, M. Sun, Q. Huang, X. Li, Z. Xu, W. Wang and X. Bai, *Angew. Chem., Int. Ed.*, 2015, **54**, 15222–15225.
- 27 N. H. Bashian, M. B. Preefer, J. Milam-Guerrero, J. J. Zak, C. Sendi, S. A. Ahsan, R. C. Vincent, R. Haiges, K. A. See, R. Seshadri and B. C. Melot, *J. Mater. Chem. A*, 2020, **8**, 12623–12632.
- 28 L. Bursill and B. Hyde, *Prog. Solid State Chem.*, 1972, **7**, 177–253.
- 29 C. P. Koçer, K. J. Griffith, C. P. Grey and A. J. Morris, *Chem. Mater.*, 2020, **32**, 3980–3989.
- 30 K. J. Griffith, I. D. Seymour, M. A. Hope, M. M. Butala, L. K. Lamontagne, M. B. Preefer, C. P. Koçer, G. Henkelman, A. J. Morris, M. J. Cliffe, S. E. Dutton and C. P. Grey, *J. Am. Chem. Soc.*, 2019, **141**, 16706–16725.
- 31 M. Goga, R. Seshadri, V. Ksenofontov, P. Gutlich and W. Tremel, *Chem. Commun.*, 1999, 979–980.
- 32 C. Boyer, C. Deudon and A. Meerschaut, *C. R. Seances Acad. Sci., Ser. 2*, 1999, **2**, 93–99.
- 33 C. Boyer-Candalen, J. Derouet, P. Porcher, Y. Moëlo and A. Meerschaut, *J. Solid State Chem.*, 2002, **165**, 228–237.
- 34 S. G. Denis and S. J. Clarke, *Chem. Commun.*, 2001, 2356–2357.
- 35 S. J. Clarke, S. G. Denis, O. J. Rutt, T. L. Hill, M. A. Hayward, G. Hyett and Z. A. Gál, *Chem. Mater.*, 2003, **15**, 5065–5072.
- 36 O. J. Rutt, T. L. Hill, Z. A. Gál, M. A. Hayward and S. J. Clarke, *Inorg. Chem.*, 2003, **42**, 7906–7911.
- 37 G. Hyett, O. J. Rutt, Z. A. Gál, S. G. Denis, M. A. Hayward and S. J. Clarke, *J. Am. Chem. Soc.*, 2004, **126**, 1980–1991.
- 38 H. Oki and H. Takagi, *Solid State Ionics*, 2015, **276**, 80–83.
- 39 R. Dovesi, A. Erba, R. Orlando, C. M. Zicovich-Wilson, B. Civalleri, L. Maschio, M. Rérat, S. Casassa, J. Baima, S. Salustro and B. Kirtman, *Wiley Interdiscip. Rev.: Comput. Mol. Sci.*, 2018, **8**, e1360.
- 40 J. P. Perdew, A. Ruzsinszky, G. I. Csonka, O. A. Vydrov, G. E. Scuseria, L. A. Constantin, X. Zhou and K. Burke, *Phys. Rev. Lett.*, 2008, **100**, 136406.
- 41 J. Heyd, G. E. Scuseria and M. Ernzerhof, *J. Chem. Phys.*, 2003, **118**, 8207–8215.



- 42 J. Heyd and G. E. Scuseria, *J. Chem. Phys.*, 2004, **121**, 1187–1192.
- 43 S. Grimme, J. Antony, S. Ehrlich and H. Krieg, *J. Chem. Phys.*, 2010, **132**, 154104.
- 44 C. Pisani, *J. Mol. Struct.: THEOCHEM*, 2003, **621**, 141–147.
- 45 H. J. Monkhorst and J. D. Pack, *Phys. Rev. B: Solid State*, 1976, **13**, 5188–5192.
- 46 K. McColl and F. Corà, *J. Mater. Chem. A*, 2019, **7**, 3704–3713.
- 47 K. McColl and F. Corà, *Phys. Chem. Chem. Phys.*, 2019, **21**, 7732–7744.
- 48 P. D'Arco, S. Mustapha, M. Ferrabone, Y. Noël, M. D. L. Pierre and R. Dovesi, *J. Phys.: Condens. Matter*, 2013, **25**, 355401.
- 49 K. Momma and F. Izumi, *J. Appl. Crystallogr.*, 2011, **44**, 1272–1276.
- 50 B. J. Morgan, *J. Open Source Softw.*, 2017, **2**, 247.
- 51 B. J. Morgan, *R. Soc. Open Sci.*, 2017, **4**, 170824.
- 52 Q. Wang, M. Nakabayashi, T. Hisatomi, S. Sun, S. Akiyama, Z. Wang, Z. Pan, X. Xiao, T. Watanabe, T. Yamada, N. Shibata, T. Takata and K. Domen, *Nat. Mater.*, 2019, **18**, 827–832.
- 53 C. P. Koçer, K. J. Griffith, C. P. Grey and A. J. Morris, *J. Am. Chem. Soc.*, 2019, **141**, 15121–15134, PMID: 31448601.
- 54 H. Sabrowsky, P. Mertens and A. Thimm, *Z. Kristallogr. - Cryst. Mater.*, 1985, **171**, 1–6.
- 55 M. Wenger and T. Armbruster, *Eur. J. Mineral.*, 1991, **3**, 387–400.
- 56 U. Olsher, R. M. Izatt, J. S. Bradshaw and N. K. Dalley, *Chem. Rev.*, 1991, **91**, 137–164.
- 57 L. R. De Jesus, J. L. Andrews, A. Parija and S. Banerjee, *ACS Energy Lett.*, 2018, **3**, 915–931.
- 58 G. A. Horrocks, A. Parija, L. R. De Jesus, L. Wangoh, S. Sallis, Y. Luo, J. L. Andrews, J. Jude, C. Jaye, D. A. Fischer, D. Prendergast, L. F. J. Piper and S. Banerjee, *Chem. Mater.*, 2017, **29**, 10386–10397.
- 59 Z. Rong, R. Malik, P. Canepa, G. Sai Gautam, M. Liu, A. Jain, K. Persson and G. Ceder, *Chem. Mater.*, 2015, **27**, 6016–6021.
- 60 B. Xu and S. Meng, *J. Power Sources*, 2010, **195**, 4971–4976.
- 61 M. Liu, Z. Rong, R. Malik, P. Canepa, A. Jain, G. Ceder and K. A. Persson, *Energy Environ. Sci.*, 2015, **8**, 964–974.
- 62 H. Fang and P. Jena, *Proc. Natl. Acad. Sci. U. S. A.*, 2017, **114**, 11046–11051.
- 63 Y. Wang, W. D. Richards, S. P. Ong, L. J. Miara, J. C. Kim, Y. Mo and G. Ceder, *Nat. Mater.*, 2015, **14**, 1026–1031.
- 64 P. Canepa, G. Sai Gautam, D. C. Hannah, R. Malik, M. Liu, K. G. Gallagher, K. A. Persson and G. Ceder, *Chem. Rev.*, 2017, **117**, 4287–4341.
- 65 J. L. Andrews, A. Mukherjee, H. D. Yoo, A. Parija, P. M. Marley, S. Fakra, D. Prendergast, J. Cabana, R. F. Klie and S. Banerjee, *Chem*, 2018, **4**, 564–585.
- 66 I. D. Johnson, G. Nolis, K. McColl, Y. A. Wu, D. Thornton, L. Hu, H. D. Yoo, J. W. Freeland, F. Corà, J. K. Cockcroft, I. P. Parkin, R. F. Klie, J. Cabana and J. A. Darr, *Inorg. Chem.*, 2020, **59**, 9783–9797.
- 67 M. Lopez, H. D. Yoo, L. Hu, J. L. Andrews, S. Banerjee and J. Cabana, *ACS Energy Lett.*, 2020, **5**, 3357–3361.
- 68 R. Wang, C.-C. Chung, Y. Liu, J. L. Jones and V. Augustyn, *Langmuir*, 2017, **33**, 9314–9323, PMID: 28732164.
- 69 H. Yaghoobnejad Asl and A. Manthiram, *Chem. Mater.*, 2019, **31**, 2296–2307.
- 70 C. P. Koçer, K. J. Griffith, C. P. Grey and A. J. Morris, *Phys. Rev. B*, 2019, **99**, 075151.
- 71 C. R. A. Catlow, *Solid State Ionics*, 1983, **8**, 89–107.
- 72 R. E. Howard and A. B. Lidiard, *Rep. Prog. Phys.*, 1964, **27**, 161–240.
- 73 G. E. Murch, *Philos. Mag. A*, 1981, **44**, 699–709.
- 74 G. E. Murch, *Solid State Ionics*, 1981, **5**, 117–120, Proceedings of the International Conference on Fast Ionic Transport in Solids.
- 75 G. E. Murch, *Solid State Ionics*, 1982, **7**, 177–198.
- 76 R. J. Friauf, *J. Appl. Phys.*, 1962, **33**, 494–505.
- 77 J. R. Dahn, W. R. McKinnon, R. R. Haering, W. J. L. Buyers and B. M. Powell, *Can. J. Phys.*, 1980, **58**, 207–213.
- 78 J. L. Andrews, *et al.*, *J. Am. Chem. Soc.*, 2018, **140**, 17163–17174.
- 79 J. Cho, A. Sheng, N. Suwandarantne, L. Wangoh, J. L. Andrews, P. Zhang, L. F. J. Piper, D. F. Watson and S. Banerjee, *Acc. Chem. Res.*, 2019, **52**, 645–655.
- 80 K. Maeda and K. Domen, *J. Phys. Chem. C*, 2007, **111**, 7851–7861.
- 81 D. D. Fan, H. J. Liu, L. Cheng, J. Zhang, P. H. Jiang, J. Wei, J. H. Liang and J. Shi, *Phys. Chem. Chem. Phys.*, 2017, **19**, 12913–12920.
- 82 H. Eschrig, A. Lankau and K. Koepf, *Phys. Rev. B: Condens. Matter Mater. Phys.*, 2010, **81**, 155447.
- 83 A. Ishikawa, T. Takata, J. N. Kondo, M. Hara, H. Kobayashi and K. Domen, *J. Am. Chem. Soc.*, 2002, **124**, 13547–13553.
- 84 G. J. Limburn, M. J. P. Stephens, B. A. D. Williamson, A. Iborra-Torres, D. O. Scanlon and G. Hyett, *J. Mater. Chem. A*, 2020, **8**, 19887–19897.
- 85 Q. D. Gibson, *et al.*, *J. Am. Chem. Soc.*, 2020, **142**, 847–856.

